AD-A279 483

PL-TR-94-2003

INVESTIGATIONS OF JOINT SEISMIC AND ELECTROMAGNETIC METHODS FOR NUCLEAR TEST MONITORING

Charles B. Archambeau
John B. Davies
Jeffrey L. Orrey

University of Colorado
Department of Physics / TAGG
Campus Box 583
Boulder, CO 80309

31 December, 1993

Final Report
September 1990-December 1993

APPROVED FOR PUBLIC RELEASE; DISTRIBUTION UNLIMITED

PHILLIPS LABORATORY
Directorate of Geophysics
AIR FORCE MATERIEL COMMAND
HANSCOM AIR FORCE BASE, MA 01731-3010

The views and conclusions contained in this document are those of the authors and should not be interpreted as representing the official policies, either express or implied, of the Air Force or the U.S. Government.

This technical report has been reviewed and is approved for publication.

JAMES F. LEWKOWICZ
Contract Manager
Solid Earth Geophysics Branch
Earth Sciences Division

JAMES F. LEWKOWICZ
Branch Chief
Solid Earth Geophysics Branch
Earth Sciences Division

JAMES F. LEWKOWICZ, Acting Director
Earth Sciences Division

This report has been reviewed by the ESC Public Affairs Office (PA) and is releasable to the National Technical Information Service (NTIS).

Qualified requestors may obtain additional copies from the Defense Technical Information Center. All others should apply to the National Technical Information Service.

If your address has changed, or if you wish to be removed from the mailing list, or if the addressee is no longer employed by your organization, please notify PL/TSI, 29 Randolph Road, Hanscom AFB, MA 01731-3010. This will assist us in maintaining a current mailing list.

Do not return copies of this report unless contractual obligations or notices on a specific document requires that it be returned.

REPORT DOCUMENTATION PAGE

Form Approved
OMB No. 0704-0188

1. AGENCY USE ONLY *(Leave blank)*

2. REPORT DATE
31December 1993

3. REPORT TYPE AND DATES COVERED
Final Report (Sept. 1990 - Dec. 1993)

4. TITLE AND SUBTITLE
Investigations of Joint Seismic and Electromagnetic Methods for Nuclear Test Monitoring

5. FUNDING NUMBERS
F19628-90-K-0051
PE 62101F
PR 7600
TA 09
WUBJ

6. AUTHOR(S)
Charles B. Archambeau
John B. Davies
Jeffrey L. Orrey

7. PERFORMING ORGANIZATION NAME(S) AND ADDRESS(ES)
University of Colorado
Dept. of Physics/TAGG
Campus Box 583
Boulder, CO 80309

8. PERFORMING ORGANIZATION REPORT NUMBER
AFPL-SR-2

9. SPONSORING/MONITORING AGENCY NAME(S) AND ADDRESS(ES)
Phillips Laboratory
29 Randolph Road
Hanscom AFB, MA 01731-3010

Contract Manager: James Lewkowicz/GPEH

10. SPONSORING/MONITORING AGENCY REPORT NUMBER
PL-TR-94-2003

11. SUPPLEMENTARY NOTES

12a. DISTRIBUTION/AVAILABILITY STATEMENT
approved for public release;
distribution unlimited

12b. DISTRIBUTION CODE

13. ABSTRACT *(Maximum 200 words)* This study is designed to develop both linear and non-linear modeling methods for prediction of excitation of atmospheric and seismic disturbances from near surface explosions and earthquake sources in complex media which include strong lateral variability, randomness and non-linear response effects. Comparisons with observations are systematically pursued to evaluate these models and to develop source discrimination methods. In this report we describe examples of non-linear atmospheric excitation by near surface explosions which are carried to ionospheric heights in order to predict fluctuations in ionospheric electron densities and ionization layer positions. These predictions are compared to active EM monitoring by ground stations of ionospheric layer perturbations due to the large amplitude atmospheric waves from surface explosions. We also consider atmospheric turbulent couplin at the earth's free surface and investigate the high frequency seismic noise characteristics resulting from this source using combined seismic and atmospheric modeling. Results are in first order agreement with spectral observations of high frequency noise, in that both the theoretical and observed particle velocity spectra vary as 1/f in the high frequency range from 1 to 50Hz. Examples of the effects of randomness large scale lateral variations and near source surface topography on the seismic wave field from near surface explosions are systematically investigated. We find good firs order correlations of predictions with the complex regional and near field observations using reasonable structure/topographic models.

14. SUBJECT TERMS
Discrimination of Seismic Sources
Seismic Waves
3-D Modeling
Atmospheric Modeling
Ionospheric Waves
Seismic Noise

15. NUMBER OF PAGES
78

16. PRICE CODE

17. SECURITY CLASSIFICATION OF REPORT	18. SECURITY CLASSIFICATION OF THIS PAGE	19. SECURITY CLASSIFICATION OF ABSTRACT	20. LIMITATION OF ABSTRACT
Unclassified	Unclassified	Unclassified	SAR

INVESTIGATIONS OF JOINT SEISMIC AND ELECTROMAGETIC METHODS FOR NUCLEAR TEST MONITORING

Table of Contents

1. Introduction

The approach to seismic source discrimination through the joint use of seismic, direct acoustic and indirect atmospheric wave sensing using electromagnetic measurements (passive or active) is illustrated in Table 1. Here seismic events of different types, made comparable by normalizing to the same low frequency compressional wave amplitude, are compared in terms of qualitative estimates of the amplitude of the different diagnostic signals relative to noise background. These relative signal amplitudes are indicated in the columns under each source type as being "large", "moderate" or "small" relative to the typical noise level. These estimates are based on seismic observations (*e.g.*, Evernden *et. al.*, 1986) and ionospheric acoustic wave measurements using EM sensing (*e.g.*, Blanc, 1982), together with rough estimates for excitation of secondary ionospheric EM emissions and the direct near surface acoustic or gravity wave. The expected "signatures" of the sources in terms of the rough sizes of the various signals are also indicated, along with the basis for discriminating between the different source types.

In order to assess quantitative signal levels, we have developed and applied atmospheric modeling methods to provide a basis for discrimination of seismic events using a combination of electromagnetic and seismic sensing methods to identify small chemical and nuclear tests, as well as earthquakes. The primary objective of the research has been to predict low frequency gravity waves in the atmosphere, produced by surface and buried explosions, that propagate to high altitudes and produce large amplitude waves in the ionosphere. Since these waves, which increase in amplitude with altitude because of the decreasing density of the atmosphere with height, will produce relatively large fluctuations in the electron densities in the ionosphere, the disturbance can be sensed by standard electromagnetic sounding techniques. Hence sensitive monitoring of explosion produced atmospheric disturbances can be accomplished by EM sounding methods. Our objective is therefore to provide predictions of the ionospheric disturbances to be expected from different kinds of shallow seismic sources so that the characteristic atmospheric wave signatures of these sources can be used, along with seismic methods, to help identify them. We also use the current nonlinear atmospheric modeling capability to systematically study coupling between near surface atmospheric turbulence and seismic noise, in a variety of earth models, in order to more fully understand and predict high frequency seismic noise variability in different geologic environments.

Another principal objective of this research has been to provide predictions of complete local and regional seismic wave fields to be expected from explosions (single and multiple) and shallow earthquakes in complex, laterally varying two and three dimensional anelastic earth models. In this work, particular importance was placed on achieving predictive capabilities over the seismic frequency band from .02Hz to 5Hz, where representation to relatively high frequencies, at or above 5Hz, was considered to be of major importance in view of the low magnitude events that are of primary interest for regional seismic discrimination. On the other hand, the lower frequency end of the range is important in the prediction of atmospheric coupling, particularly for estimating the excitation of low frequency gravity waves.

Achieving results that are close to the observed complexity of seismic wave fields, through incorporation of vertical and lateral randomness, rough topography and abrupt lateral changes in crust-upper mantle seismic velocity structure was considered important for seismic discrimination, with some of this medium variability being important in characterizing atmospheric wave excitation as well. To obtain realistic estimates major effort involved development and application of different 2 and 3-D numerical modeling methods to quantify the

TABLE 1.

Multiple Field Discrimination of Small Seismic Events
A List of Expected Qualitative Differences

Discriminatory Signal Type	Small ($m_b < 4$) Event Types, all with the same "low" frequency seismic P wave Amplitude			
	Tamped Nuclear Test	Decoupled Nuclear Test	Industrial Explosion	Shallow Earthquake
Regional High Frequency (f > 10) Seismic P wave Signal (Relative amplitude)	Moderate / Large	Large	Small / Moderate	Small
Near - Regional Acoustic Signal (Relative amplitude)	Small / Undetectible	Undetectible	Large	Undetectible
Ionospheric E-M Sounding (Relative amplitude)	Small	Undetectible	Large	Small / Undetectible
Secondary Ionospheric E-M Emissions (Relative amplitude)	Small	Undetectible	Large	Small / Undetectible
	signature: M/L, S/U, S, S	signature: L, U, U, U	signature: S/M, L, L, L	signature: S, U, S/U, S/U

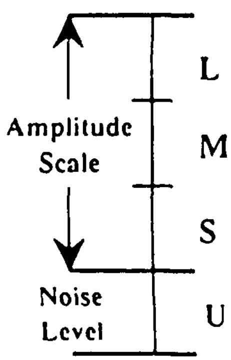

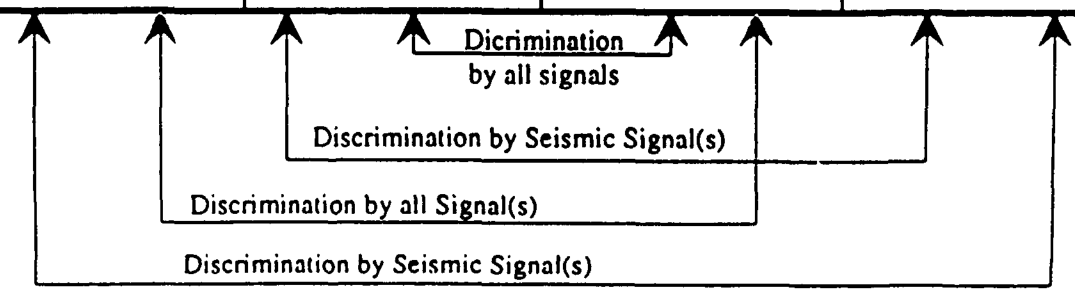

mechanisms of generation of discriminatory signals and to quantify their variability as functions of changes in 3-D earth structure and source type.

2. Modeling Seismic Signal Propagation in the Near and Regional Distance Ranges

2.1. Numerical Methods for Seismic Wavefield Modeling

Most modeling of seismic wavefields in laterally heterogeneous media has used spatially discrete numerical methods such as the finite difference or finite element technique. The main reason for using a pseudospectral method instead of these conventional techniques is the increased accuracy of a pseudospectral approximation, which allows for larger scale and/or higher frequency simulations. The pseudospectral method actually belongs to a larger class of discretization techniques known as spectral methods. The significance of the nomenclature is explained below. Comparisons have been made between finite difference and Fourier pseudospectral methods in terms of runtimes, memory requirements and accuracy of solutions [6] [3] [14]. The general conclusion is that for two-dimensional simulations of the same wavefield, a fourth-order finite difference method currently runs about twice as fast as a Fourier method, but requires about twice the memory. Of course a specific comparison between methods requires the consideration of how they incorporate the following factors, among others: sources, absorbing boundaries, anelastic attenuation, material structure sampling, a free surface condition, and machine vectorization and concurrency. Although no firm conclusions have been drawn for three-dimensional problems, storage requirements alone favor the use of spectral methods for large calculations. This has led us to investigate their usefulness for both 2-D and 3-D modeling.

The spectral methods we are investigating solve the elastodynamic equations of motion by approximating the spatial dependencies as truncated series of orthogonal functions and by integrating the expansion coefficients in time as in a finite difference method. We derive the method from a variational formulation of momentum conservation, and we include a free surface boundary condition by making the spatial domain nonperiodic. Although solving nonperiodic problems is usually computationally much more costly than periodic problems that use harmonic functions, our method requires little more computation than the Fourier method, and it accurately simulates surface waves.

2.2. Variational Formulation of Spectral Methods

In the equations that follow, Greek subscripts denote spatial coordinate directions, and $\mathbf{n}_\beta$ is a unit vector in the β direction. Boldface subscripts and superscripts on summations represent three-dimensional sets of integers, e.g. $\mathbf{k} = (k_1, k_2, k_3)$, so that $\sum_{\mathbf{k}}$ represents a triple sum. Summation over repeated indices is assumed, and the symbol i represents $\sqrt{-1}$.

For a spectral solution to the elastodynamic equations of motion, we expand each component of the displacement field in a truncated series of infinitely differentiable, orthogonal basis functions $b(\mathbf{k}, \mathbf{x})$ over the volume $V_{\mathbf{X}} = \prod_{\beta=1}^{3} X_\beta$ of the spatial domain:

$$u_\alpha(\mathbf{x}, t) = \sum_{\mathbf{k}=-\mathbf{K}/2}^{\mathbf{K}/2} b(\mathbf{k}, \mathbf{x})\, \hat{U}_\alpha(\mathbf{k}, t) \tag{1}$$

Let the symbols $\langle\ \rangle$, $\{\ \}$, and $[\quad]$ denote a row vector, column vector, and square matrix, respectively, so that equation (1) may be written as

$$u_\alpha(\mathbf{x}, t) = \langle b(\mathbf{x})\rangle \{\hat{U}_\alpha(t)\} \tag{2}$$

From orthogonality, the wavenumber coefficients are

$$\{\hat{U}_\alpha(t)\} = \int_{V_{\mathbf{X}}} \langle b^*(\mathbf{x})\rangle u_\alpha(\mathbf{x}, t)\, d^3x \tag{3}$$

With a strain field

$$\epsilon_{\alpha\beta}(\mathbf{x},t) = \frac{1}{2}\left(\langle \frac{\partial}{\partial x_\beta} b(\mathbf{x})\rangle\{\hat{U}_\alpha(t)\} + \langle \frac{\partial}{\partial x_\alpha} b(\mathbf{x})\rangle\{\hat{U}_\beta(t)\}\right) \tag{4}$$

we consider a general constitutive relation and express the stress tensor as

$$\sigma_{\alpha\beta}(\mathbf{x},t) = E_{\alpha\beta\delta\gamma}(\mathbf{x})\epsilon_{\alpha\beta}(\mathbf{x},t) \tag{5}$$

In order to obtain a governing equation for the coefficients $\hat{U}_\alpha(t)$, we substitute the expansions of equations (2), (4), and (5) into the variational statement of momentum conservation:

$$\int_{V_\mathbf{x}} [\, \rho(\mathbf{x}) \frac{\partial^2}{\partial t^2}\mathbf{u}(\mathbf{x},t) \cdot \delta\mathbf{u}^*(\mathbf{x}) + \underline{\sigma}(\mathbf{x},t) \cdot \delta\underline{\epsilon}^*(\mathbf{x}) - \mathbf{f}(\mathbf{x},t) \cdot \delta\mathbf{u}^*(\mathbf{x}) \,]\, d^3x$$

$$- \oint_{S_t} \mathbf{t}(\mathbf{x},t) \cdot \delta\mathbf{u}^*(\mathbf{x})\, dS \;=\; 0 \tag{6}$$

where $\delta\mathbf{u}(\mathbf{x})$ is a virtual displacement, $\delta\epsilon(\mathbf{x})$ is a virtual strain, and a * indicates a complex conjugate. $f_\alpha(\mathbf{x},t)$ is a body force density and the surface integral is taken over that part of the surface on which the tractions $t_\alpha(\mathbf{x},t)$ are applied. We express the result as

$$\{\delta\hat{U}_\alpha\}^\dagger(\, [\hat{M}]\{ \frac{\partial^2}{\partial t^2}\hat{U}_\alpha(t)\} + [\hat{K}_{\alpha\delta}]\{\hat{U}_\delta(t)\} - \{\hat{F}_\alpha(t)\}\,) = 0 \tag{7}$$

where

$$[\hat{M}] = \int_{V_\mathbf{x}} \langle b(\mathbf{x})\rangle^\dagger \rho(\mathbf{x}) \langle b(\mathbf{x})\rangle d^3x \tag{8}$$

$$[\hat{K}_{\alpha\delta}] = \int_{V_\mathbf{x}} \langle \frac{\partial}{\partial x_\beta} b(\mathbf{x})\rangle^\dagger E_{\alpha\beta\delta\gamma}(\mathbf{x}) \langle \frac{\partial}{\partial x_\gamma} b(\mathbf{x})\rangle d^3x \tag{9}$$

$$\{\hat{F}_\alpha(t)\} = \int_{V_\mathbf{x}} \langle b(\mathbf{x})\rangle^\dagger f_\alpha(\mathbf{x},t) d^3x + \oint_{S_t} \langle b(\mathbf{x})\rangle^\dagger t_\alpha(\mathbf{x},t) dS \tag{10}$$

and a † represents conjugate transpose. The null vector is the only vector orthogonal to all virtual (unconstrained) displacements, so we have as a governing equation

$$[\hat{M}]\{ \frac{\partial^2}{\partial t^2}\hat{U}_\alpha(t)\} + [\hat{K}_{\alpha\beta}]\{\hat{U}_\beta(t)\} - \{\hat{F}_\alpha(t)\} = 0 \tag{11}$$

Before choosing a particular basis set $\langle b(\mathbf{x})\rangle$, let us change the formulation slightly in anticipation of the numerical solution. It is convenient to keep the stress tensor explicit in order to apply anelastic attenuation in the time domain as per Emmerich and Korn [4] or Witte and Richards [16]. To that end, we express the restoring force

$$\{\hat{R}_\alpha(t)\} = [\hat{K}_{\alpha\delta}]\{\hat{U}_\delta(t)\} \tag{12}$$

in terms of the stress tensor by expanding the stress tensor with the basis functions:

$$\sigma_{\alpha\beta}(\mathbf{x}, t) = \langle b(\mathbf{x})\rangle\{\hat{T}_{\alpha\beta}(t)\} \tag{13}$$

Expressions for the coefficients $\{\hat{T}_{\alpha\beta}(t)\}$ in terms of displacement and moduli coefficients are obtained by comparing equation (13) to equation (5) once a particular constitutive relation is chosen. In practice, we solve two first-order partial differential equations for stress and velocity and write momentum conservation as

$$[\hat{M}]\{\frac{\partial}{\partial t}\hat{V}_\alpha(t)\} + [\hat{D}_\beta]\{\hat{T}_{\alpha\beta}(t)\} - \{\hat{F}_\alpha(t)\} = 0 \tag{14}$$

where $\{\frac{\partial}{\partial t}\hat{V}_\alpha(t)\}$ is a vector of velocity coefficients and $[\hat{D}_\beta]$ is the divergence matrix:

$$[\hat{D}_\beta] = \int_{V_\mathbf{x}} \langle \frac{\partial}{\partial x_\beta} b(\mathbf{x})\rangle^\dagger \langle b(\mathbf{x})\rangle d^3x \tag{15}$$

Given a constitutive relation and an appropriate set of basis functions, we can obtain explicit equations for the expansion coefficients $\hat{V}_\alpha(t)$ and $\hat{T}_{\alpha\beta}(t)$. In what follows, consider as a special case isotropic material whose modulus is given by

$$E_{\alpha\beta\delta\gamma}(\mathbf{x}) = \lambda(\mathbf{x})\,\delta_{\alpha\beta}\delta_{\delta\gamma} + \mu(\mathbf{x})\,(\delta_{\alpha\delta}\delta_{\beta\gamma} + \delta_{\alpha\gamma}\delta_{\delta\beta}) \tag{16}$$

In general, however, no restrictions are placed on the symmetry of the medium. The density and Lamé coefficients are expanded in the chosen basis, e.g.

$$E_{\alpha\beta\delta\gamma}(\mathbf{x}) = \sum_{\mathbf{k}=-\mathbf{K}/2}^{\mathbf{K}/2} \hat{E}_{\alpha\beta\delta\gamma}(\mathbf{k})\, b(\mathbf{x},\mathbf{k}) \tag{17}$$

and the integrals in equations (8), (10), and (15) are solved by invoking orthogonality.

2.3. Boundary Conditions

Because equation (14) for momentum conservation was obtained from a variational principle, the natural boundary conditions on the surface of the domain are automatically satisfied. In the absence of the surface integral in equation (10), a traction-free boundary condition is implicit in the formulation, but the basis functions themselves must allow the free surface condition. In the Fourier spectral method, the basis functions are sines and cosines over the interval 2π in each coordinate direction, and therefore the boundary conditions are periodic. On the other hand, a traction-free boundary corresponds to a nonperiodic problem. For nonperiodic problems, the basis functions must be nonperiodic, as are Chebychev or Legendre polynomials. Chebychev polynomials have been used successfully to solve the free surface condition in elasticity [11], but the method is not derived from a variational principal. Using a variational formulation ensures that the stiffness matrix of equation (9) is Hermitian positive semi-definite and hence the eigenvalues of this differential operator are real and non-negative. It is well known that spectral methods for non-periodic domains lead to non-Hermitian matrices [1]. If one were to use a variational formulation with a Chebychev basis set, the integrals in equations (8), (10), and (15) could not be evaluated by invoking orthogonality, and such a formulation would be computationally prohibitive. Because the differential operator of a Chebychev spectral method possesses complex eigenvalues, a simple leapfrog time integration scheme is not stable, and a fourth-order Runge Kutta scheme is usually employed. The boundary conditions are made stable by adding additional constraints based on characteristic variables [1]. The computational effort using this scheme for a problem with a given spatial domain size is four times that of a simple leapfrog method for the same problem, and it réquires four levels of storage. Kosloff, et. al. [10] have recently developed a high-order time integration method referred to as the Rapid Expansion Method, which may improve the efficiency of the Chebychev method while eliminating numerical dispersion entirely. However, they note that time histories must be kept in storage, which seems to be a prohibitive requirement.

2.4. The Fourier Sawtooth Method

Our approach to incorporating a free surface condition into a spectral method has been to use a basis set comprised of harmonic functions (the Fourier method), plus additional terms in the vertical direction that will decouple the ends of the otherwise periodic spatial domain. We use a basis set that maintains orthogonality so that the scheme is computationaly efficient and can be solved with a simple low-order time integration method. Polynomials have been used with Fourier series to improve the convergence for nonperiodic problems [8], but they have not been included in a variational formulation. We consider here a Fourier set plus a linear term. The linear term's spatial dependence is that of a sawtooth minus the Fourier representation of the sawtooth. With this form the sawtooth function is orthogonal to all Fourier terms. Its spatial dependence is illustrated in Figure (1). Applying this mixed basis set to the variational formulation of the previous section, we derive expressions in two dimensions, but the derivation is easily extended to 3-D.

Let the field variables' expansion be

$$v_\alpha(\mathbf{x},t) = \sum_{\mathbf{k}=-\mathbf{K}/2}^{\mathbf{K}/2} b(\mathbf{k},\mathbf{x})\,\hat{V}_\alpha(\mathbf{k},t) + \sum_{k_1=-K_1/2}^{K_1/2} b(k_1,I,\mathbf{x})\,\hat{V}_\alpha(k_1,I,t) \tag{18}$$

where

$$b(\mathbf{k},\mathbf{x}) = e^{i2\pi k_\beta x_\beta/X_\beta} \tag{19}$$

and

$$b(k_1,I,\mathbf{x}) = e^{i2\pi k_1 x_1/X_1}\Big[\frac{x_2}{X_2} - \Big(\frac{1}{2} + \frac{i}{2\pi}\sum_{k_2\neq 0}\frac{1}{k_2}\,e^{i2\pi k_2 x_2/X_2}\Big)\Big] \tag{20}$$

with normalization

$$|b(k_1,I,\mathbf{x})| = V_X \mathrm{B}_I \qquad ; \qquad \mathrm{B}_I = \frac{1}{12} - \sum_{k_2\neq 0}\frac{1}{(2\pi k_2)^2} \tag{21}$$

The index I indicates terms associated with the x_2 dependence of the sawtooth minus the Fourier representation of the sawtooth. With this form $b(k_1,I,\mathbf{x})$ is orthogonal to $b(\mathbf{k},\mathbf{x})$ for all $\mathbf{k}$. From now on we neglect the limits on summations, so that the limits are implied to be those of equation (18) unless otherwise indicated. By expanding the density and Lamé coefficients in the basis functions of equations (19) and (20), and by defining

$$\hat{\rho}(k_1,I) = \hat{\rho}(k_1,0) + \frac{1}{B_I}\sum_{j_2\neq 0}\hat{\rho}(k_1,j_2)\Big[\frac{3}{8\pi^2 j_2{}^2} - \frac{1}{4\pi^2}\sum_{k_2\neq\pm j_2}\frac{1}{k_2(k_2+j_2)}\Big] \tag{22}$$

and similarly for $\hat{\lambda}(k_1,I)$ and $\hat{\mu}(k_1,I)$, equation (14) in the absence of body forces becomes

$$\sum_{\mathbf{l}}\hat{\rho}(\mathbf{k}-\mathbf{l})\frac{\partial}{\partial t}\hat{V}_1(\mathbf{l},t) = \frac{i2\pi k_1}{X_1}\hat{T}_{11}(\mathbf{k},t) + \frac{i2\pi k_2}{X_2}\hat{T}_{12}(\mathbf{k},t) \tag{23}$$

$$\sum_{\mathbf{l}}\hat{\rho}(\mathbf{k}-\mathbf{l})\frac{\partial}{\partial t}\hat{V}_2(\mathbf{l},t) = \frac{i2\pi k_1}{X_1}\hat{T}_{12}(\mathbf{k},t) + \frac{i2\pi k_2}{X_2}\hat{T}_{22}(\mathbf{k},t) \tag{24}$$

$$\sum_{l_1}\hat{\rho}(k_1-l_1,I)\frac{\partial}{\partial t}\hat{V}_1(l_1,I,t) = \frac{i2\pi k_1}{X_1}\hat{T}_{11}(k_1,I,t) - \frac{1}{B_I X_2}\sum_{l_2}\hat{T}_{12}(k_1,l_2,t) \tag{25}$$

$$\sum_{l_1}\hat{\rho}(k_1-l_1,I)\frac{\partial}{\partial t}\hat{V}_2(l_1,I,t) = \frac{i2\pi k_1}{X_1}\hat{T}_{12}(k_1,I,t) - \frac{1}{B_I X_2}\sum_{l_2}\hat{T}_{22}(k_1,l_2,t) \tag{26}$$

The stress tensor coefficients are obtained from the constitutive relation:

$$\frac{\partial}{\partial t}\hat{T}_{11}(\mathbf{k},t) = \sum_{\mathbf{l}}\Big[\Big(\hat{\lambda}(\mathbf{k}-\mathbf{l})+2\hat{\mu}(\mathbf{k}-\mathbf{l})\Big)\frac{i2\pi l_1}{X_1}\hat{V}_1(\mathbf{l},t) + \hat{\lambda}(\mathbf{k}-\mathbf{l})\Big(\frac{i2\pi l_2}{X_2}\hat{V}_2(\mathbf{l},t)+\frac{1}{X_2}\hat{V}_2(l_1,I,t)\Big)\Big] \tag{27}$$

$$\frac{\partial}{\partial t}\hat{T}_{12}(\mathbf{k},t) = \sum_{\mathbf{l}}\Big[\hat{\mu}(\mathbf{k}-\mathbf{l})\frac{i2\pi l_1}{X_1}\hat{V}_2(\mathbf{l},t) + \hat{\mu}(\mathbf{k}-\mathbf{l})\Big(\frac{i2\pi l_2}{X_2}\hat{V}_1(\mathbf{l},t)+\frac{1}{X_2}\hat{V}_1(l_1,I,t)\Big)\Big] \tag{28}$$

$$\frac{\partial}{\partial t}\hat{T}_{22}(\mathbf{k},t) = \sum_{\mathbf{l}}\Big[\hat{\lambda}(\mathbf{k}-\mathbf{l})\frac{i2\pi l_1}{X_1}\hat{V}_1(\mathbf{l},t) + \Big(\hat{\lambda}(\mathbf{k}-\mathbf{l})+2\hat{\mu}(\mathbf{k}-\mathbf{l})\Big)\Big(\frac{i2\pi l_2}{X_2}\hat{V}_2(\mathbf{l},t)+\frac{1}{X_2}\hat{V}_2(l_1,I,t)\Big)\Big] \tag{29}$$

$$\frac{\partial}{\partial t}\hat{T}_{11}(k_1,I,t) = \sum_{l_1}\Big(\hat{\lambda}(k_1-l_1,I)+2\hat{\mu}(k_1-l_1,I)\Big)\frac{i2\pi l_1}{X_1}\hat{V}_1(l_1,I,t) \tag{30}$$

$$\frac{\partial}{\partial t}\hat{T}_{12}(k_1,I,t) = \sum_{l_1}\hat{\mu}(k_1-l_1,I)\frac{i2\pi l_1}{X_1}\hat{V}_2(l_1,I,t) \tag{31}$$

$$\frac{\partial}{\partial t}\hat{T}_{22}(k_1,I,t) = \sum_{l_1}\hat{\lambda}(k_1-l_1,I)\frac{i2\pi l_1}{X_1}\hat{V}_1(l_1,I,t) \tag{32}$$

Notice that products in the spatial domain have become convolutions in the wavenumber domain. Their general form is

$$\hat{T}(\mathbf{k}) = \sum_{\acute{\mathbf{k}}}\hat{E}(\mathbf{k}-\acute{\mathbf{k}})\,\hat{\epsilon}(\acute{\mathbf{k}}) \tag{33}$$

and they typically are computed with a Fast Fourier Transform (FFT). The computational efficiency of the FFT precludes the use of any other (current) methods for performing the convolutions. The wavenumber coefficients for the velocity and stress fields are obtained by numerically integrating equations (23) - (32) in time.

2.5. *The Collocation or Pseudospectral Method*

If we solve the governing equations in the spatial domain instead of in the wavenumber domain, both domains are discretized. The two domains are related by a discrete Fourier series. Such a treatment is called a collocation method, but it is also referred to as a pseudospectral method for reasons described below. Note that the material moduli and density already are sampled at discrete points in space by using an FFT to perform the convolutions of the previous section.

Let the continuous space $\mathbf{x} = x_\beta \mathbf{n}_\beta$ be discretized into the positions $j_\beta \Delta x_\beta \mathbf{n}_\beta$, with N_β collocation points evenly spaced by a distance Δx_β along the direction β. The wavenumbers become discretized as $\frac{2\pi k_\beta}{X_\beta}\mathbf{n}_\beta$ for $k_\beta = -N_\beta/2+1, ..., N_\beta/2$, and $X_\beta = N_\beta \Delta x_\beta$. The spatially discretized velocity is

$$v_\alpha(j_\beta \Delta x_\beta \mathbf{n}_\beta, t) \equiv V_\alpha(\mathbf{j}, t) = \sum_{\mathbf{k}=-\mathbf{N}/2+1}^{\mathbf{N}/2} \tilde{V}_\alpha(\mathbf{k}, t)\, e^{i2\pi k_\beta j_\beta / N_\beta} \qquad ; \qquad j_\beta = 0, ..., N_\beta - 1 \tag{34}$$

where the index $k_\beta = N_\beta/2$ corresponds to both of the identical positive and negative Nyquist frequencies along the direction β. The symbol for the expansion coefficient has been changed from $\hat{V}$ to $\tilde{V}$ to distinguish its relationship to the spatial domain. While $\hat{V}$ is found from equation (3), $\tilde{V}$ is found from the discrete orthogonality relation

$$\frac{1}{N}\sum_{k=0}^{N-1} e^{i2\pi kj/N} = \begin{cases} 1 & \text{if } j = nN; n = 0, \pm1, \pm2, ... \\ 0 & \text{otherwise} \end{cases} \tag{35}$$

so that the expansion coefficients are obtained from a discrete transform:

$$\tilde{V}_\alpha(\mathbf{k}, t) = \frac{1}{V_\mathrm{N}} \sum_{\mathbf{j}=0}^{\mathbf{N}-1} V_\alpha(\mathbf{j}, t)\, e^{-i2\pi k_\beta j_\beta / N_\beta} \qquad ; \qquad V_\mathrm{N} \equiv \prod_{\gamma=1}^{3} \mathrm{N}_\gamma \tag{36}$$

The continuum field is represented by the N/2-degree trigonometric interpolant of the nodal quantities of equation (34).

$$v_\alpha(\mathbf{x}, t) = \sum_{\mathbf{k}=-\mathbf{N}/2+1}^{\mathbf{N}/2} \tilde{V}_\alpha(\mathbf{k}, t)\, e^{i2\pi k_\delta x_\delta / X_\delta} \tag{37}$$

Field derivatives in the discrete space are defined in terms of this continuous field:

$$\frac{\partial}{\partial x_\beta} v_\alpha(\mathbf{x}, t) = \sum_{\mathbf{k}} \tilde{V}_\alpha(\mathbf{k}, t)(i2\pi k_\beta)\, e^{i2\pi k_\delta x_\delta / X_\delta} \tag{38}$$

so that

$$\frac{\partial}{\partial x_\beta} V_\alpha(\mathbf{k}, t) = \sum_{\mathbf{k}} \tilde{V}_\alpha(\mathbf{k}, t)(i2\pi k_\beta)\, e^{i2\pi k_\delta j_\delta / N_\delta} \tag{39}$$

The discrete Fourier expansion coefficients $\tilde{V}_\alpha(\mathbf{k}, t)$ may be regarded as approximations to the continuum field coefficients $\hat{V}_\alpha(\mathbf{k}, t)$ of the previous section, where the trapezoidal rule is used to evaluate the integral in the inverse transform.

The stress field will be aliased if the resulting bandwidth of the convolution sum in (33) exceeds the bandwidth of the basis set used to synthesize the spatial domain stress and strain fields. Let the spatial strain field be composed of a total of N_β nonzero wavenumbers in the direction β. Since we require that the stress and strain fields have the same bandwidth, the indices $\mathbf{k}$ and $\acute{\mathbf{k}}$ in equation (33) have the same range. The range of the index difference $k_\beta - \acute{k}_\beta$ on the modulus is then $-N_\beta$ to N_β, and a stress field bandlimited to $\pm N_\beta/2$ wavenumbers samples the modulus spectrum up to $\pm N_\beta$ wavenumbers. If the bandwidth of the modulus exceeds $\pm N_\beta$, then the convolution in (33) will be aliased. For the collocation method, aliasing from the convolution cannot be avoided if the bandwidths of the material structure and the wavefield are the same. The term pseudospectral was used by Orszag [12] to describe such a method, because with aliasing the method is not a complete spectral method. Since our differential equations are linear in the absence of external forces, however, the error of one wavenumber does not affect the error of another wavenumber, and aliasing errors in the pseudospectral method are insignificant for wavefields with most of their energy below about half the Nyquist sampling frequency, i.e. wavelengths less than about four grid spaces [15].

To obtain a collocation formulation of the Fourier-Sawtooth method, apply the discrete transform to equations (23) -(32) to obtain the following governing equations:

$$\rho(\mathbf{j})\,\frac{\partial}{\partial t}V_1(\mathbf{j},t) \;=\; \sum_{\mathbf{k}}\Big[\,\frac{i2\pi k_1}{X_1}\,\tilde{T}_{11}(\mathbf{k},t)+\frac{i2\pi k_2}{X_2}\,\tilde{T}_{12}(\mathbf{k},t)\,\Big]\,e^{i2\pi k_\beta j_\beta/N_\beta} \tag{40}$$

$$\rho(\mathbf{j})\,\frac{\partial}{\partial t}V_2(\mathbf{j},t) \;=\; \sum_{\mathbf{k}}\Big[\,\frac{i2\pi k_1}{X_1}\,\tilde{T}_{12}(\mathbf{k},t)+\frac{i2\pi k_2}{X_2}\,\tilde{T}_{22}(\mathbf{k},t)\Big]\,e^{i2\pi k_\beta j_\beta/N_\beta} \tag{41}$$

$$\rho(j_1,I)\,\frac{\partial}{\partial t}V_1(j_1,I,t) \;=\; \sum_{k_1}\frac{i2\pi k_1}{X_1}\,\tilde{T}_{11}(k_1,I,t)e^{i2\pi k_1 j_1/N_1}-\frac{1}{B_1X_2}\,T_{12}(j_1,0,t) \tag{42}$$

$$\rho(j_1,I)\,\frac{\partial}{\partial t}V_2(j_1,I,t) \;=\; \sum_{k_1}\frac{i2\pi k_1}{X_1}\,\tilde{T}_{12}(k_1,I,t)e^{i2\pi k_1 j_1/N_1}-\frac{1}{B_1X_2}\,T_{22}(j_1,0,t) \tag{43}$$

The constitutive relation becomes

$$\begin{aligned}\frac{\partial}{\partial t}T_{11}(\mathbf{j},t) \;&=\; \Big[\,\lambda(\mathbf{j})+2\mu(\mathbf{j})\,\Big]\sum_{\mathbf{l}}\frac{i2\pi l_1}{X_1}\,\tilde{V}_1(\mathbf{l},t)e^{i2\pi l_\beta j_\beta/N_\beta}\\ &\quad+\lambda(\mathbf{j})\,\Big[\,\sum_{\mathbf{l}}\frac{i2\pi l_2}{X_2}\tilde{V}_2(\mathbf{l},t)e^{i2\pi l_\beta j_\beta/N_\beta}+\frac{1}{\Delta x_2}V_2(j_1,I,t)\delta_{j_2}\,\Big]\end{aligned} \tag{44}$$

$$\begin{aligned}\frac{\partial}{\partial t}T_{12}(\mathbf{j},t) \;&=\; \mu(\mathbf{j})\Big[\,\sum_{\mathbf{l}}\Big(\,\frac{i2\pi l_1}{X_1}\,\tilde{V}_2(\mathbf{l},t)+\frac{i2\pi l_2}{X_2}\,\tilde{V}_1(\mathbf{l},t)\,\Big)e^{i2\pi l_\beta j_\beta/N_\beta}\\ &\quad+\frac{1}{\Delta x_2}V_1(j_1,I,t)\delta_{j_2}\,\Big]\end{aligned} \tag{45}$$

$$\begin{aligned}\frac{\partial}{\partial t}T_{22}(\mathbf{j},t) \;&=\; \lambda(\mathbf{j})\sum_{\mathbf{l}}\frac{i2\pi l_1}{X_1}\,\tilde{V}_1(\mathbf{l},t)e^{i2\pi l_\beta j_\beta/N_\beta}\\ &\quad+\Big[\lambda(\mathbf{j})+2\mu(\mathbf{j})\Big]\,\Big[\,\sum_{\mathbf{l}}\frac{i2\pi l_2}{X_2}\tilde{V}_2(\mathbf{l},t)e^{i2\pi l_\beta j_\beta/N_\beta}+\frac{1}{\Delta x_2}V_2(j_1,I,t)\delta_{j_2}\,\Big]\end{aligned} \tag{46}$$

$$\frac{\partial}{\partial t}T_{11}(j_1,I,t) \;=\; \Big[\,\lambda(j_1,I)+2\mu(j_1,I)\,\Big]\sum_{l_1}\frac{i2\pi l_1}{X_1}\,V_1(l_1,I,t)e^{i2\pi l_1 j_1/N_1} \tag{47}$$

$$\frac{\partial}{\partial t}T_{12}(j_1,I,t) \;=\; \mu(j_1,I)\sum_{l_1}\frac{i2\pi l_1}{X_1}\,V_2(l_1,I,t)e^{i2\pi l_1 j_1/N_1} \tag{48}$$

$$\frac{\partial}{\partial t}T_{22}(j_1,I,t) \;=\; \lambda(j_1,I)\sum_{l_1}\frac{i2\pi l_1}{X_1}\,V_1(l_1,I,t)e^{i2\pi l_1 j_1/N_1} \tag{49}$$

Body forces and/or surface tractions are applied as initial conditions on $V_\beta(\mathbf{j},t=0)$ and $T_{\alpha\beta}(\mathbf{j},t=0)$, and equations (40) - (49) are integrated in time with a leapfrog method whose time step is small enough to make numerical dispersion insignificant (e.g., in 1-D $C_{max}\Delta t/\Delta x \sim 0.2$). Nyquist errors are eliminated by using odd-based real-to-complex

FFTs to compute terms on the right hand sides of the equations. The required number of FFT operations is about one fourth the required number in a Chebychev pseudospectral method that uses a fourth-order Runge-Kutta time integration scheme and real-to-complex FFTs.

2.6. *Numerical Tests*

The best test of the accuracy of a numerical method's simulation of a free surface condition is a comparison of the numerical and analytic solutions to Lamb's problem: An impulsive source on the surface of a homogeneous halfspace. We have compared analytic solutions to Lamb's problem to those obtained using the Fourier-Sawtooth pseudospectral algorithm described in the previous section. For the following comparisons, the P-wave and S-wave velocities of the medium are 5 km/s and 3 km/s, respectively, with a density of 2.5 g/cm^3, and the numerical grid spacing is 1 km. For these values, the frequency of an S-wave traveling with the Nyquist wavelength of 2 km is 1.5 Hz, and the Rayleigh wave velocity is about 2.74 km/s. The source was applied as a delta function in time and space and the time series solutions were lowpass filtered to remove Gibbs truncation effects.

For a source applied directly on the surface, i.e. at $x_2 = 0$, considerable energy would be transmitted to the bottom of the grid because the basis functions cannot distinguish the boundary at $x_2 = 0$ from the boundary at $x_2 = X_2$. Figure (2) displays the normalized kinetic energy density field of the Fourier-Sawtooth solution 5.5 seconds after an impulsive source was applied at a depth of 1 km. The field has been spatially lowpass filtered to remove the Gibbs noise. The source was applied over four nodes in the middle of the side of the grid with the highest elevation in the figure. The P-wave, S-wave, and surface wave

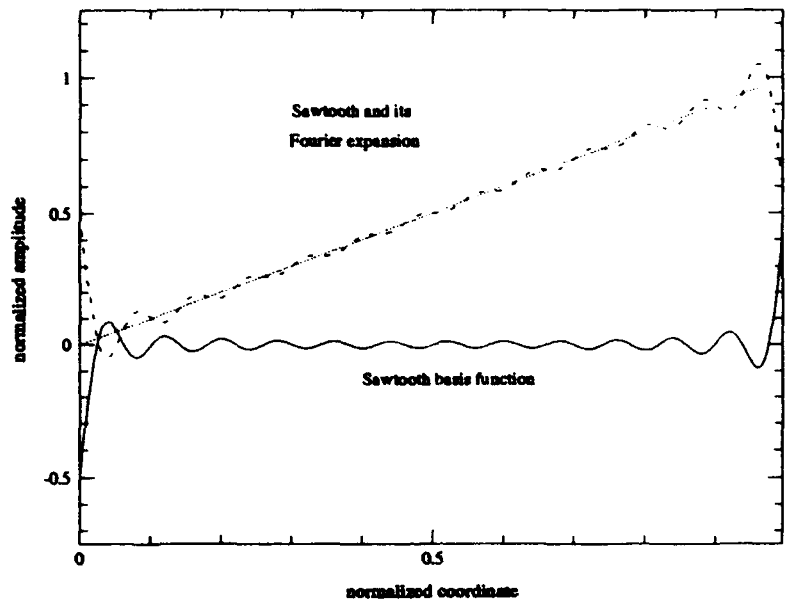

Figure 1: Sawtooth basis function. The basis function is the difference between a sawtooth and the Fourier expansion of a sawtooth.

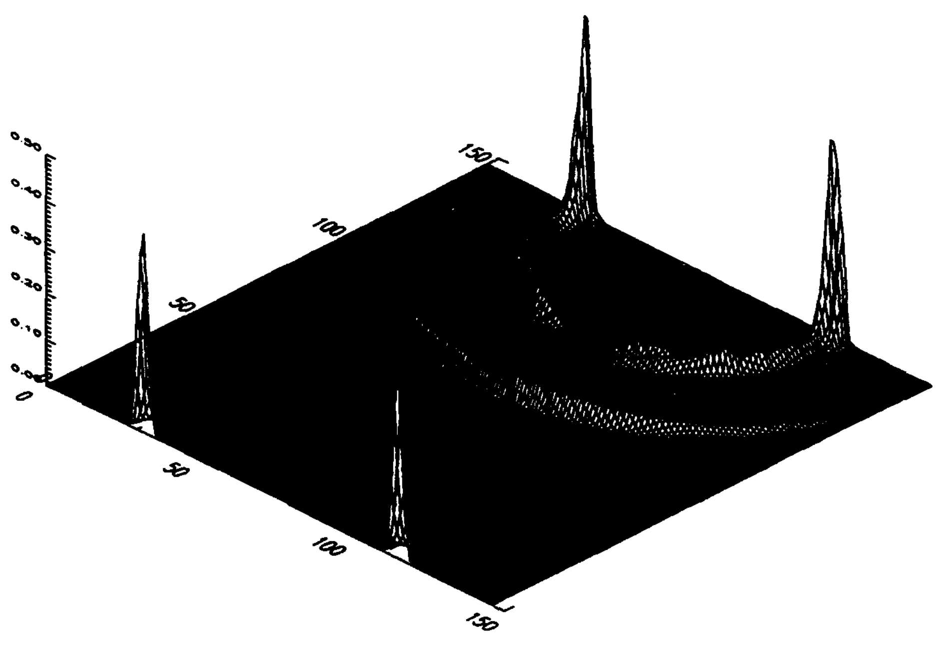

Figure 2: Normalized kinetic energy field of the Fourier-Sawtooth solution for an impulsive source at a depth of $1km$. The source was applied in the middle of the side of the grid with the highest elevation in the figure.

phases are clearly visible. Notice that the top and bottom of the grid are still coupled, and surface wave energy propogates along the bottom boundary with nearly the same amplitude as the surface waves on the top boundary. Figures (3) through (6) compare horizontal and vertical displacements from the Fourier-Sawtooth solution and a similarity solution [5] for the impulsive source at a depth of 1 km. The Fourier-Sawtooth domain has a uniform grid spacing of 1 km in each coordinate direction. The numerical solution's body wave accuracy is essentially that of the Fourier method. However, the numerical solution's Rayleigh wave is accurate near the source but becomes less accurate as the Rayleigh wave propogates away from the source. The amplitudes of both the horizontal and vertical displacement traces decrease because of the transmission of energy through the boundary, and the horizontal trace arrives very early.

The Rayleigh wave solution can be improved significantly by refining the spatial resolution of the computational domain in the vicinity of the boundary. A spatial domain with evenly spaced gridpoints is mapped to a domain that is compressed in the viscinity of the free surface, as represented in Figure (7). Grid mapping in pseudospectral computations was first introduced to improve the accuracy of locating interfaces [7]. Tal-Ezer, et. al. [13] have used a mapping to increase the grid spacing near the boundaries in a Chebychev method in order to allow for larger time integration steps. Our mapped spatial domain resembles the domain intrinsic to a Chebychev basis, but it admits a simple inverse mapping so that source and receiver positions may be specified easily. Figure (8), when compared to Figure (2), indicates that this mapping has greatly reduced the amount of surface wave energy that leaks through the boundary. The leakage is reduced for body waves also, although this is

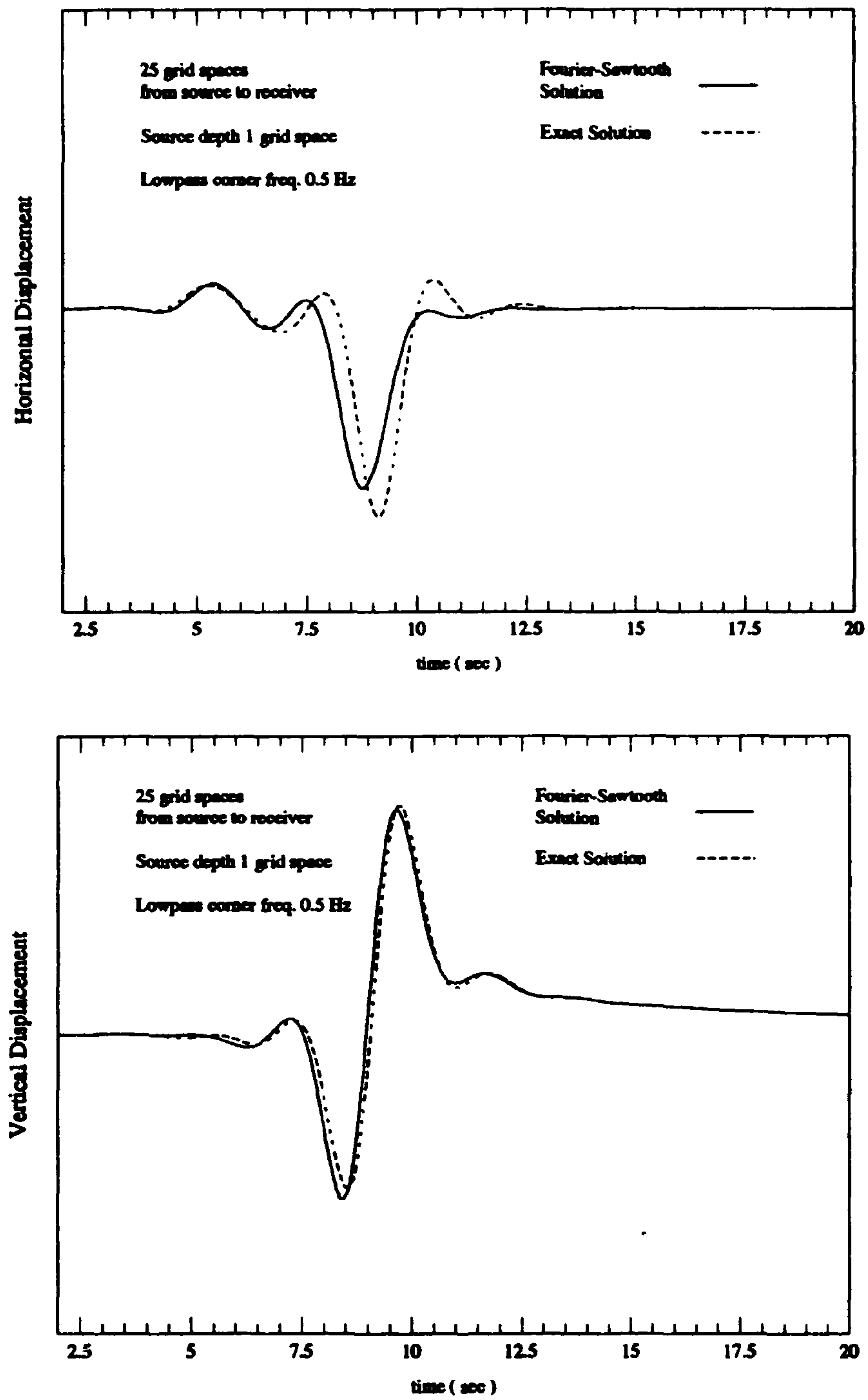

Figure 3: Comparison of horizontal and vertical displacements from the Fourier-Sawtooth solution and the analytic solution to Lamb's problem for a 1 km deep source. The horizontal and vertical grid spacings are both 1 km, the source-receiver distance is 25 km, and the solutions were lowpass filtered with a corner frequency of 0.5 Hz.

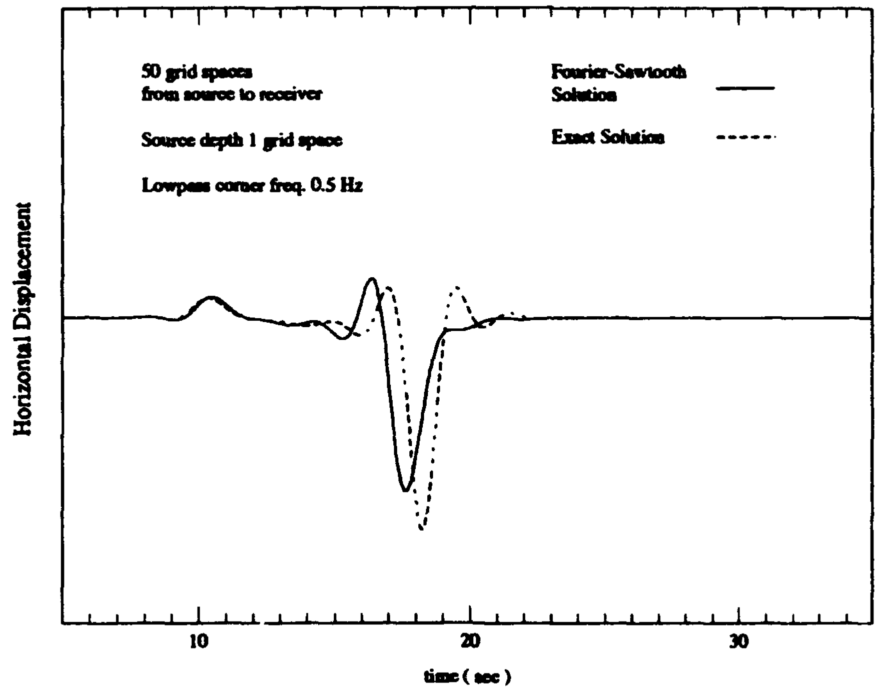

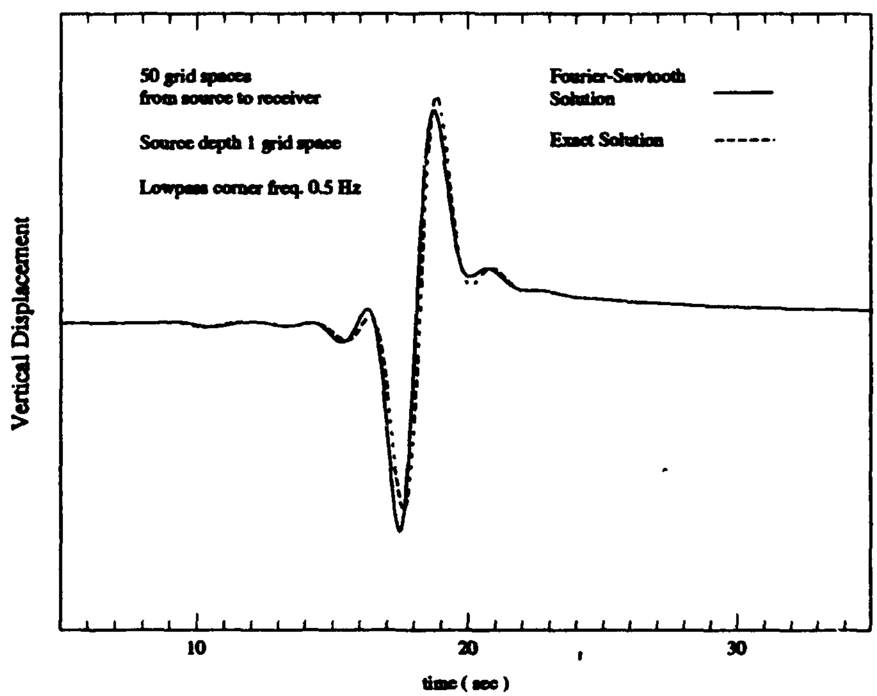

Figure 4: Same as Figure (3) except the source-receiver distance is 50 km.

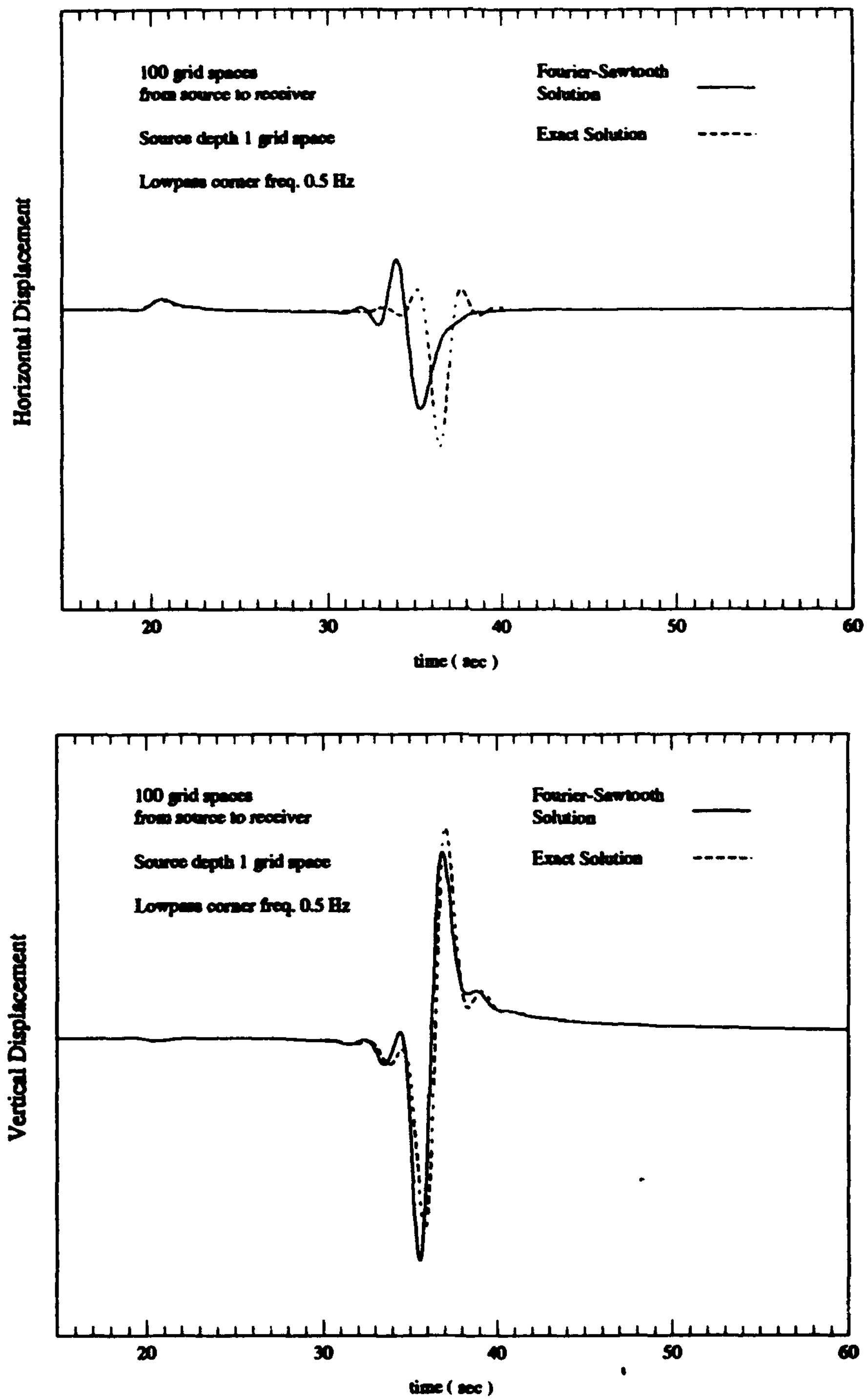

Figure 5: Same as Figure (3) except the source-receiver distance is 100 km.

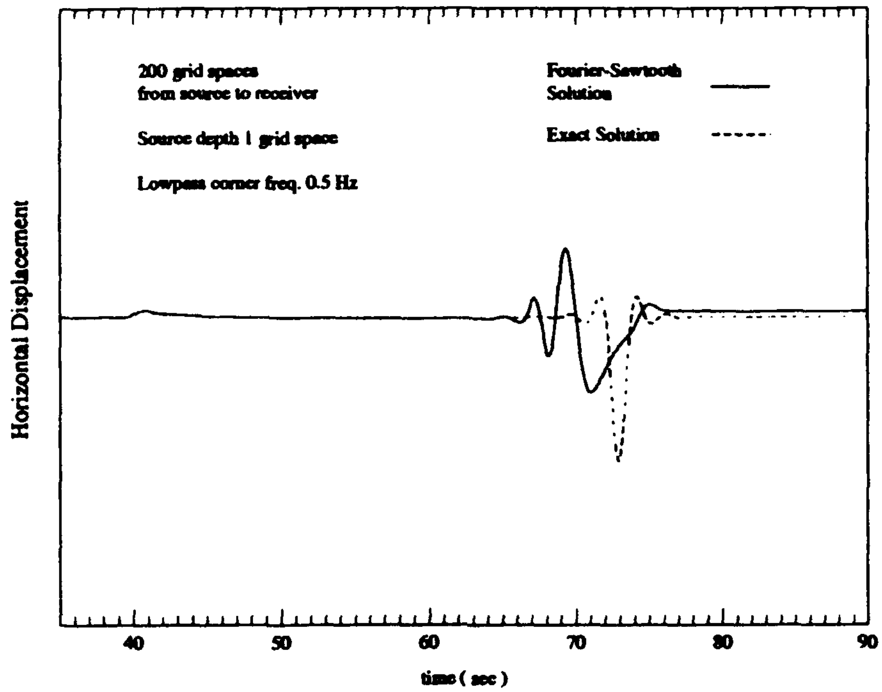

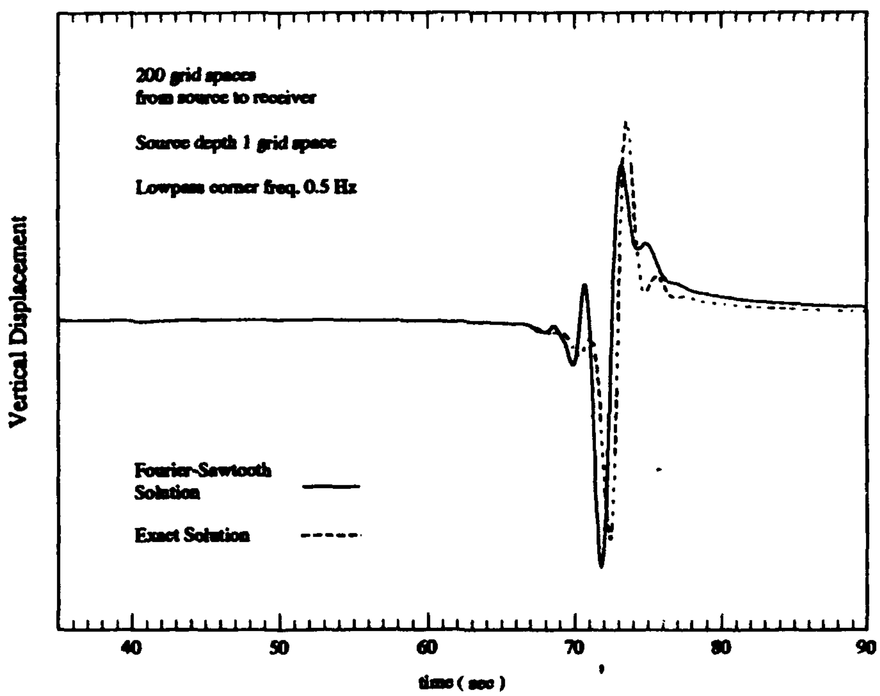

Figure 6: Same as Figure (3) except the source-receiver distance is 200 km.

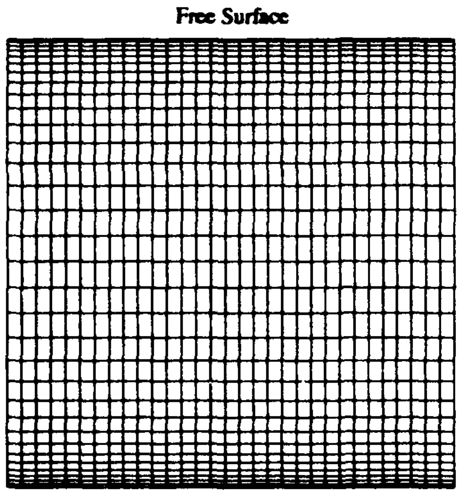

Figure 7: Spatial domain mapping to improve surface wave solutions in the Fourier-Sawtooth method.

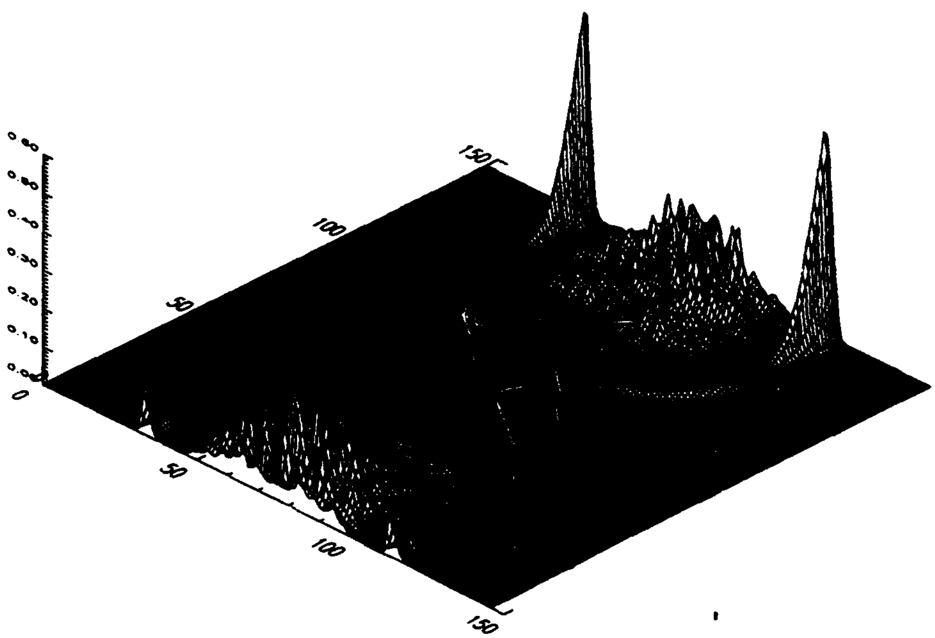

Figure 8: Same as Figure (2) except spatial domain mapped to refine the spatial resolution in the vicinity of the boundary.

not apparent given the amplitude scale of the figure. Notice that some energy in the grid is still trapped in the source region at the time of the snapshot. Because the source was applied locally in a region with relatively small grid spacings, it generated high- frequency energy that cannot be supported by the larger grid spacings at depth. These frequencies are reflected and trapped within the finer grid. The simulation used to generate Figure (8) was identical to the one for Figure (2) except for the domain mapping. The initially uniform domain with a grid spacing of 1.0 km was mapped to a domain with a minimum grid spacing of 0.20 km at the boundaries and a maximum spacing of 1.89 km at the center of the domain. Figures (9) through (12) compare displacements from the Fourier-Sawtooth and analytic solutions for a 1 km deep source and this domain mapping in the vertical direction of the numerical method. The horizontal grid spacing was kept uniform at 1 km. The horizontal displacement solution has improved significantly, and both horizontal and vertical displacement solutions decay very little with distance from the source. Both traces' arrival times are in error by slightly more than one percent. This is to be expected for an approximation method based on a variational principle. The approximate eigenvalues are slightly higher than the exact ones. In Figure (12), the amplitude mismatch after 74 seconds is due almost entirely to interference from a body wave incident from depth, as no absorbing boundaries were applied.

We have compared the Fourier-Sawtooth solution to a normal mode solution [9] for a 1 km deep explosive source in the structure shown in Figure (13). A high-velocity cap layer was included in the structure at a depth of 150 km for the normal mode simulation. Absorbing boundary conditions were applied to the Fourier-Sawtooth algorithm by the method suggested by Cerjan, et. al. [2]. The velocity and stress fields are attenuated within a zone of grid points near the boundaries, and the amount of attenuation increases as the wavefield approaches the boundaries. The results were lowpass filtered with a corner frequency of 0.5 Hz. The time series from the two methods at a source-receiver distance of 205 km are overlayed in Figure (14) to compare the surface wave dispersion, and record sections from the two algorithms are shown in Figure (15). Because the normal mode algorithm has cylindrical symmetry and the Fourier-Sawtooth method is cartesian, the relative body wave to surface wave amplitudes do not match, but the surface waves display very similar dispersion characteristics when scaled for comparison.

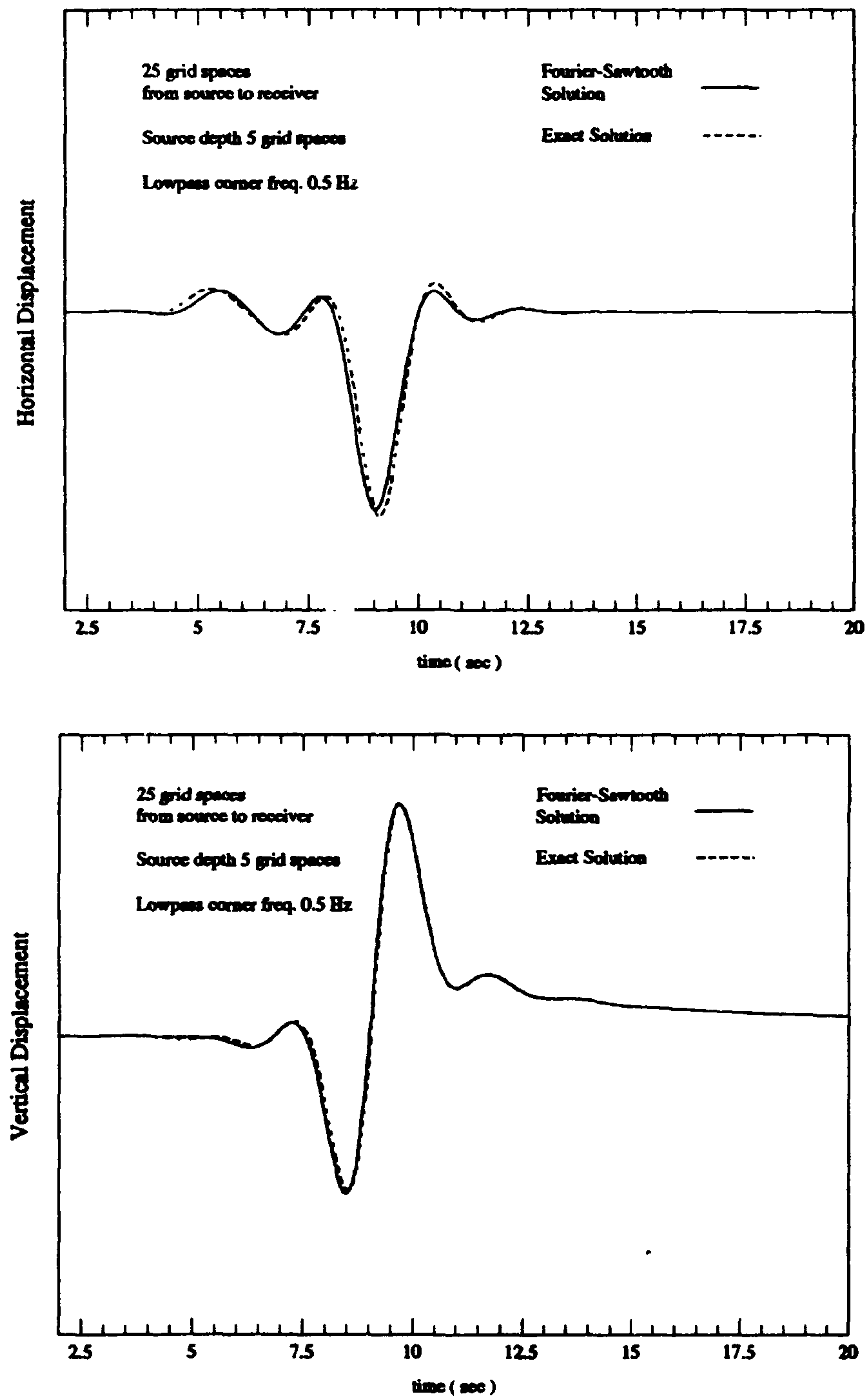

Figure 9: Comparison of horizontal and vertical displacements from the Fourier-Sawtooth solution and the analytic solution to Lamb's problem for a 1 km deep source. The horizontal grid spacing is constant at 1 km but the vertical spacing is mapped to refine the spatial resolution in the vicinity of the boundary. The source-receiver distance is 25 km, and the solutions were lowpass filtered with a corner frequency of 0.5 Hz.

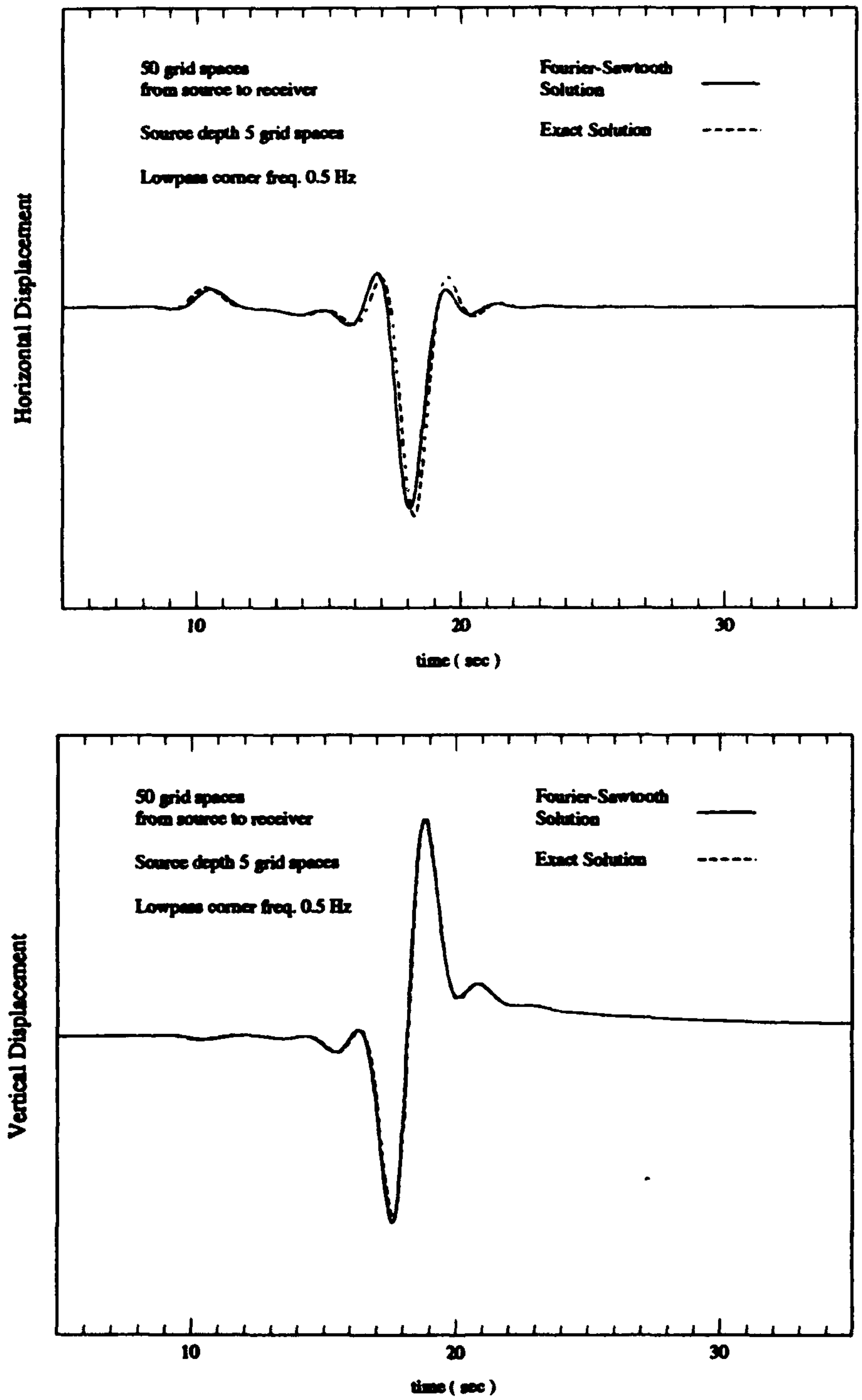

Figure 10: Same as Figure (9) except the source-receiver distance is 50 km.

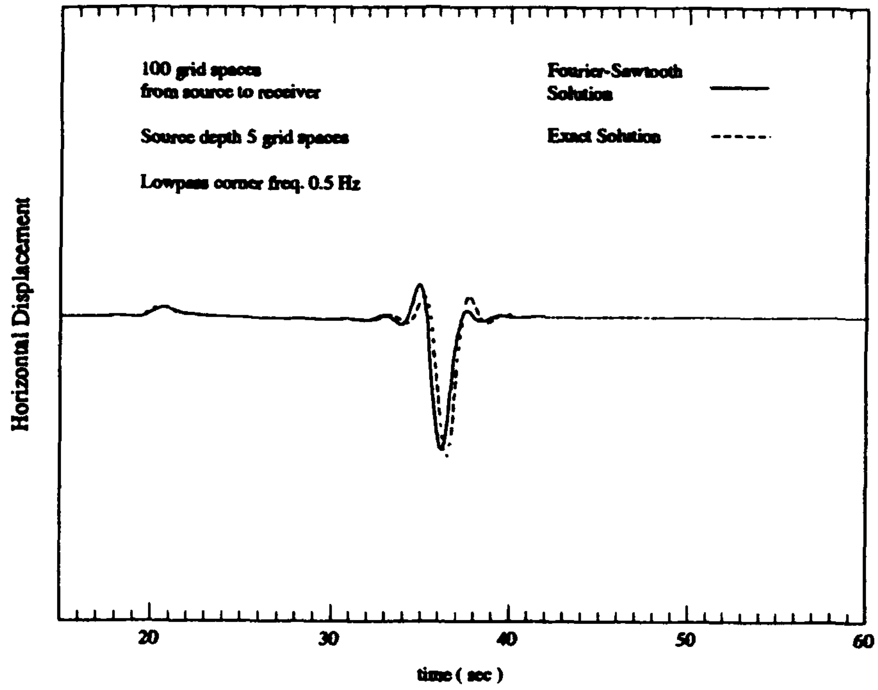

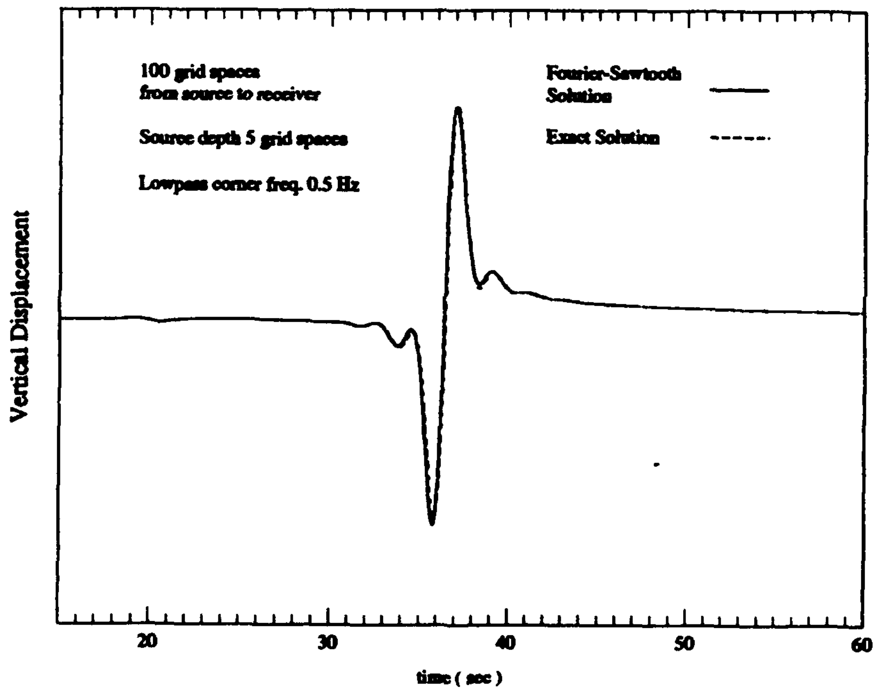

Figure 11: Same as Figure (9) except the source-receiver distance is 100 km.

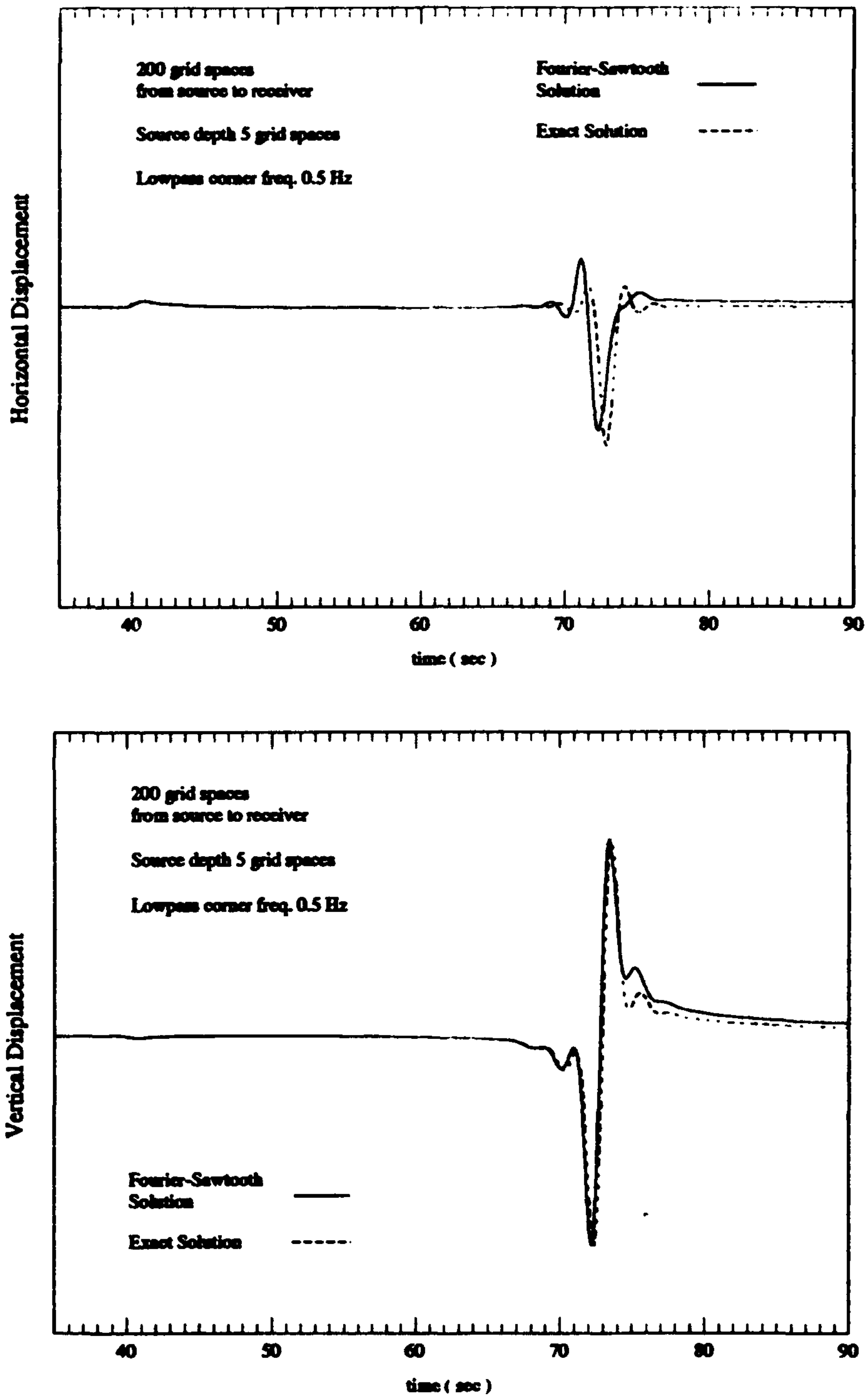

Figure 12: Same as Figure (9) except the source-receiver distance is 200 km. The amplitude mismatch after 74 seconds is due almost entirely to interference from a body wave incident from depth.

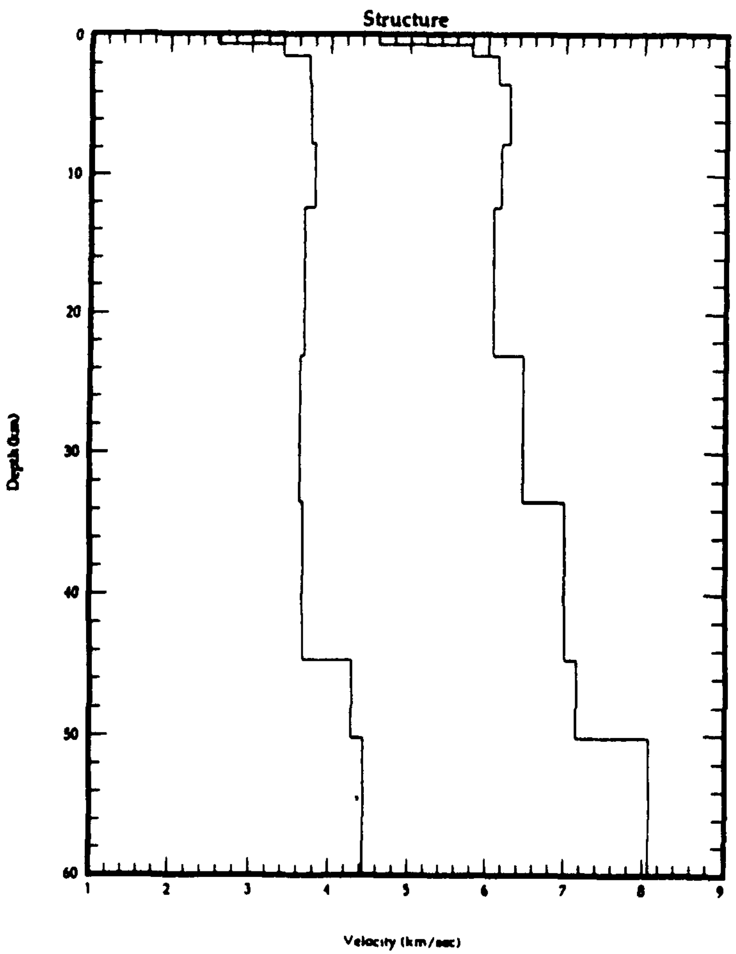

Figure (13). Structure used for Fourier-Sawtooth/Normal Mode comparison.

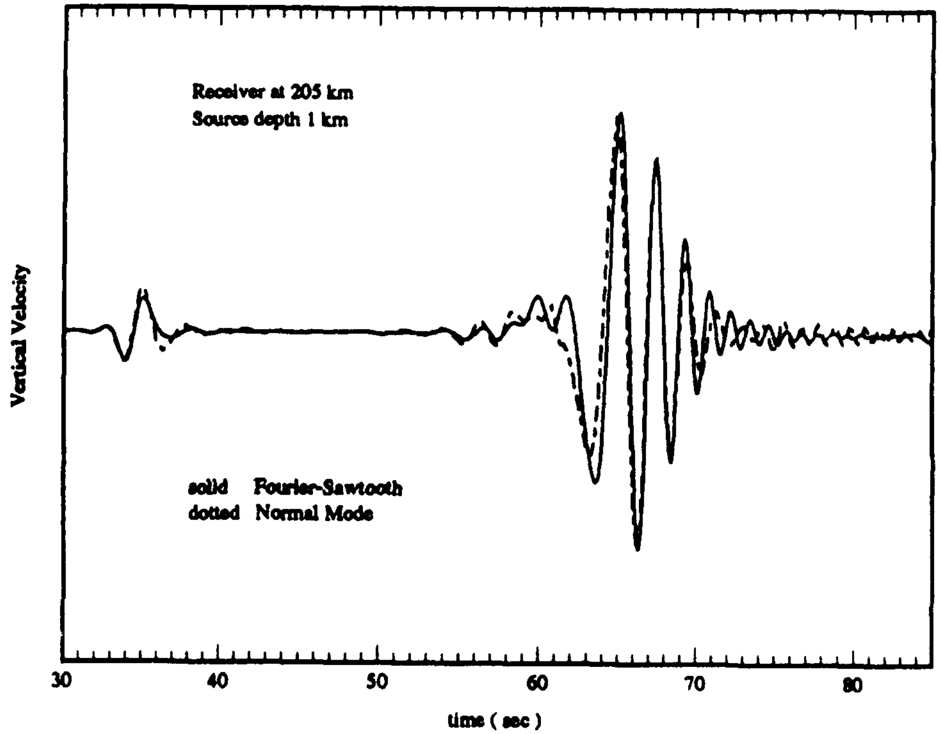

Figure (14). Time series comparison of the Fourier-Sawtooth and Normal Mode methods at a source-receiver distance of 205 km for the structure shown in Figure (13).

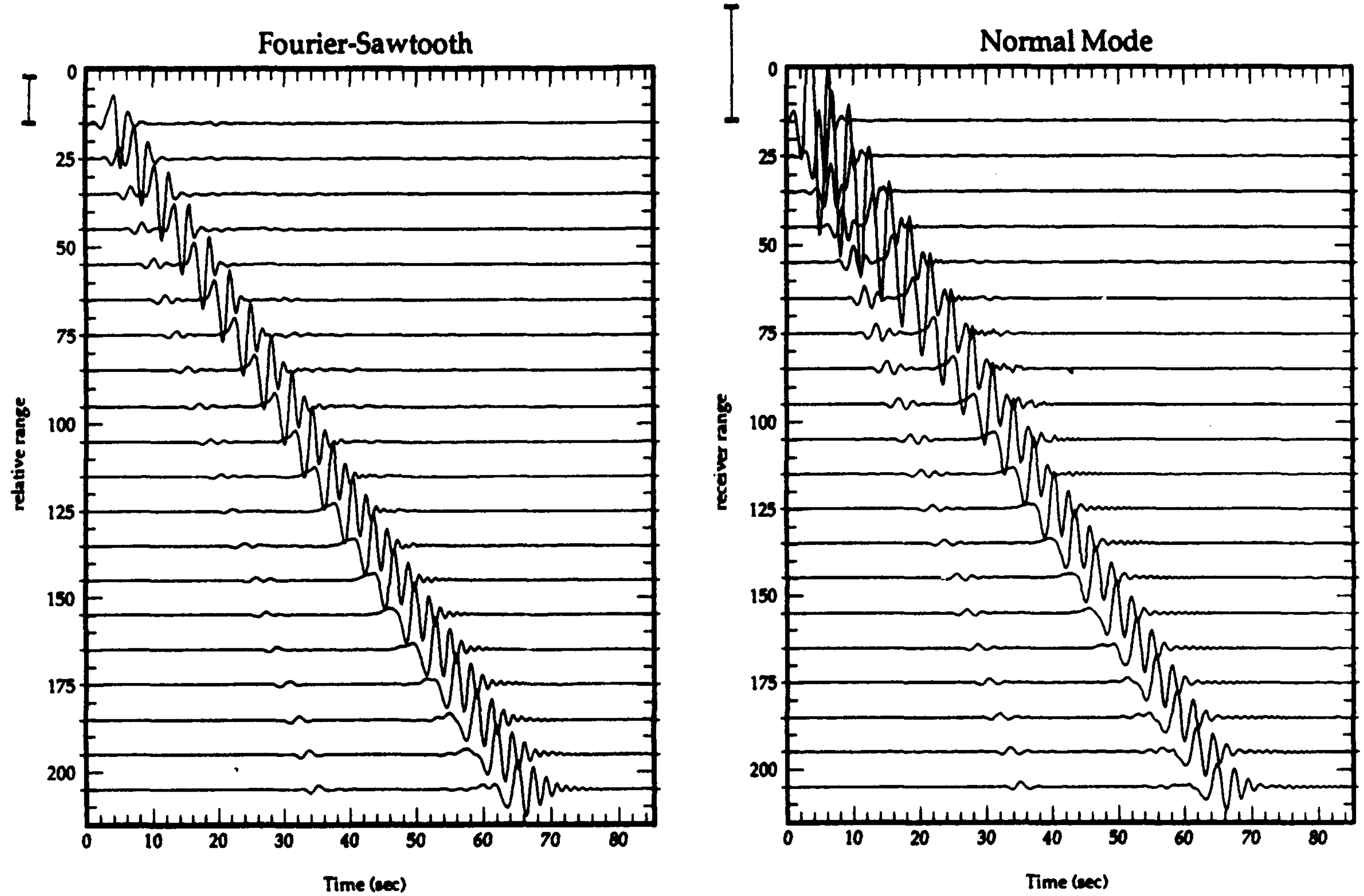

Figure (15). Record sections of the Fourier-Sawtooth and Normal Mode solutions for the structue shown in Figure (13).

2.7. *Numerical Modeling of Seismic Sources and Wave Propagation in Complex Media*

We have recently developed several numerical modeling programs that are well suited to both non-linear source modeling problems and wave propagation in elastic-anelastic or plastic media. These finite difference and finite element type programs are all operational on our Stardent computer system which allows us to perform lengthy computations in 2 and 3 dimensional grid systems. The graphics features of the Stardent are particularly valuable in displaying and understanding the results.

The particular numerical programs we have available for this study are of two classes; those that can be called the "standard" finite difference or finite element programs, and programs based on spectral or pseudospectral methods (*eg*. Carcione *et. al.* 1992, Kosloff *et. al.* 1990, Witte and Richards, 1990, Canuto *et. al.* 1988, Orszag 1971). The "spectral" programs have been developed recently (*eg*. Orrey and Archambeau, 1993) using generalizations of the earlier pseudospectral methods, as well as refinements of numerical procedures, to produce a fast, memory economic and accurate computational method for the simulation of seismic wave propagation in 2 and 3-D anelastic media.

Tests of the "full spectral" numerical method (wherein the spatial dependence of the field variables, as well as the medium structure properties, are represented in terms of Fourier basis sets) and the psuedospectral method (wherein only spatial derivatives of field variables are computed by FFT methods) have been made to check the accuracy of the methods. Our approach has been to compare these numerical results to those obtained by modal synthesis methods (*eg*. Harvey, 1981) for laterally uniform models. In this regard Figure (16) shows a comparison of synthetics produced by the analytically based modal synthesis method and those by the pseudospectral method.

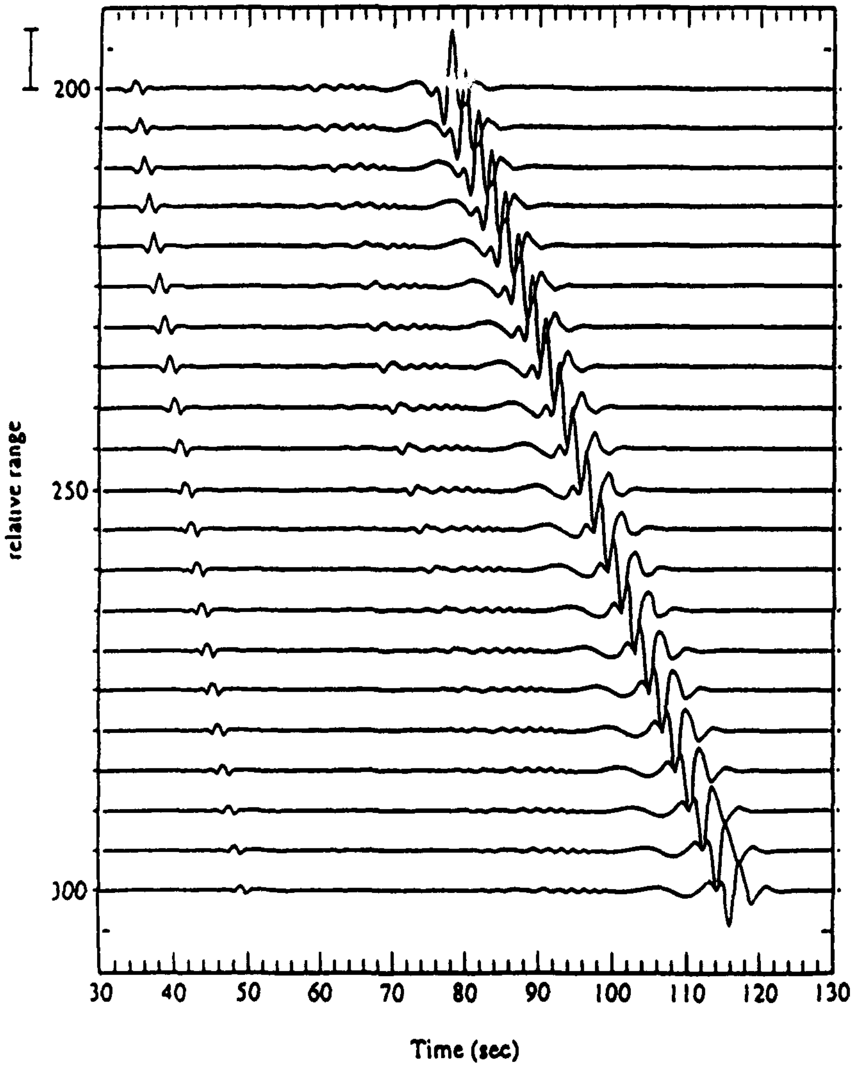

Figure 16-a. Complex pseudospectral synthetic seismograms for a layered earth structure. The Explosion source was applied at a depth of 1 km. with a maximum frequency content near 1Hz.

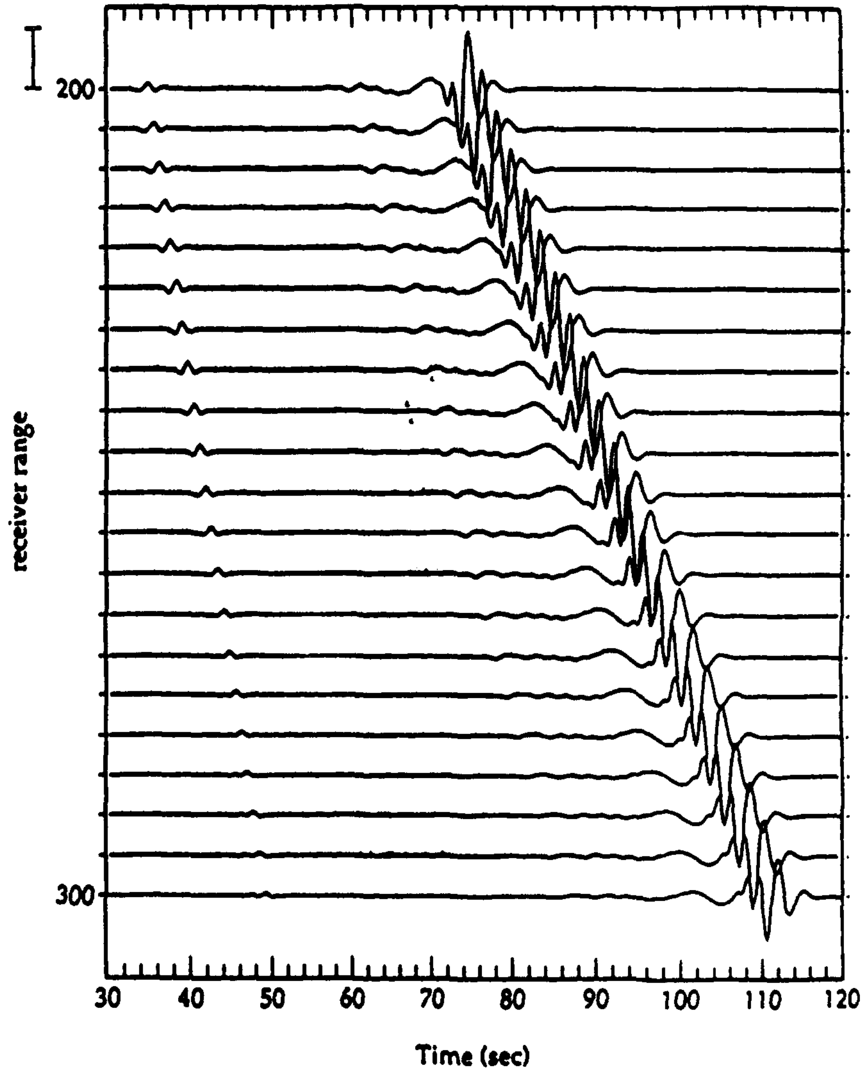

Figure 16-b. Normal mode synthetic seismograms for a layered earth structure similar to that used for Figure 16-a. The maximum frequency content is near 1Hz. The frequency content in the 16-a synthetics is slightly higher than that in these modal synthetics.

The structure used is shown in Figure (17), and is applicable to the region of the nuclear test site in Eastern Kazakhstan. Similar results are obtained using the "full spectral" method described. These tests show very good accuracy for these methods based on computational comparisons to modal (and reflectivity) methods. Consequently, we feel confident that these (new) numerical methods will also be accurate for wave propagation studies in the laterally variable 2 and 3-D models.of interest.

In this regard Figure (18) illustrates results from full 2-D tests of these modeling programs. In this example we have examined some effects of near source surface topography and fine scale layering on the seismic wave field generated by a buried explosion (depth 300 meters). The sequence of insets in Figures (18a) and (18b) shows the spatial evolution of the wave field with time following the detonation of the explosion, with the effects of topographic

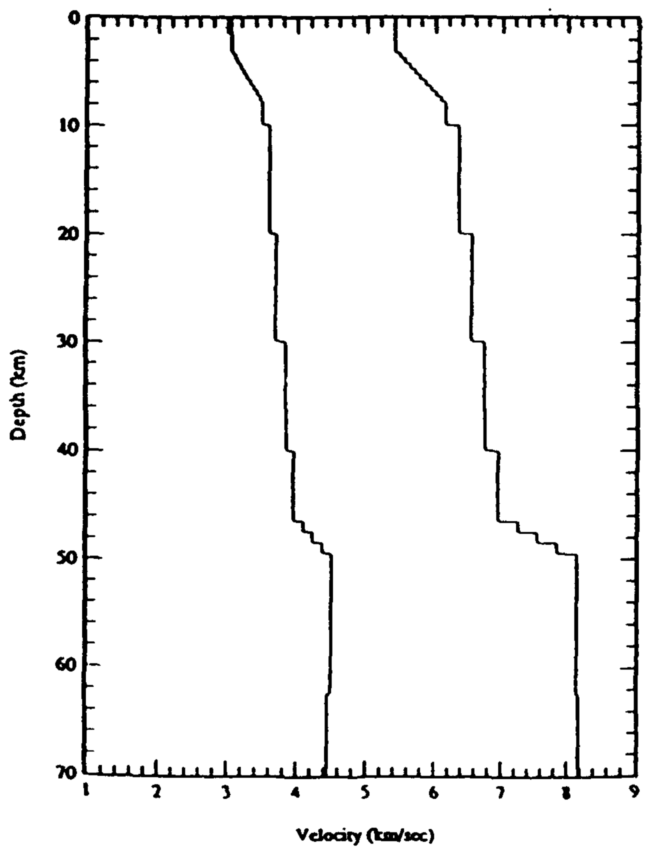

Figure 17. Layered structure used in the modeling comparisons of Figure 1.

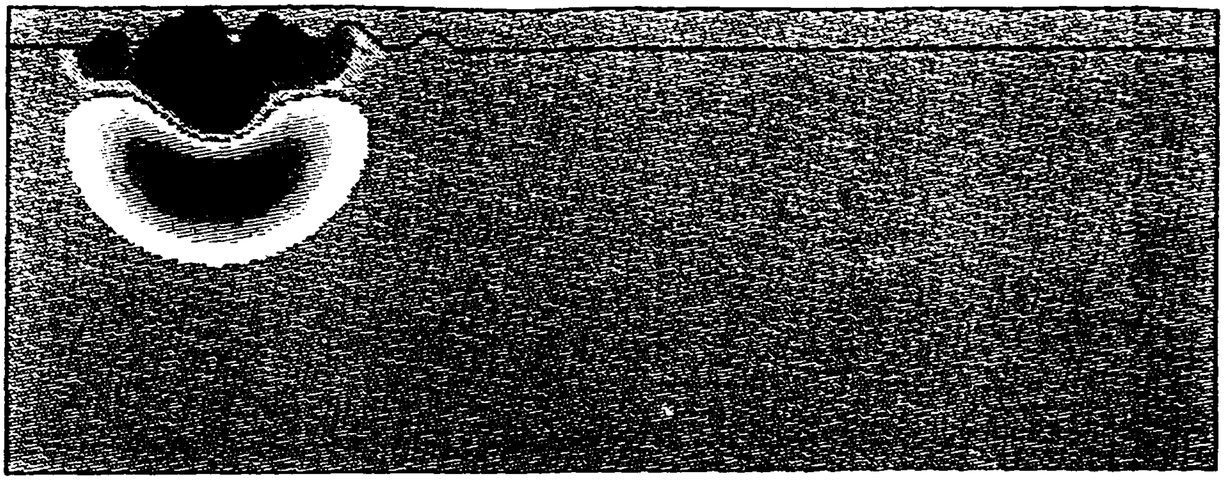

(a.) Vertical Velocity Field; .32 sec. after detonation

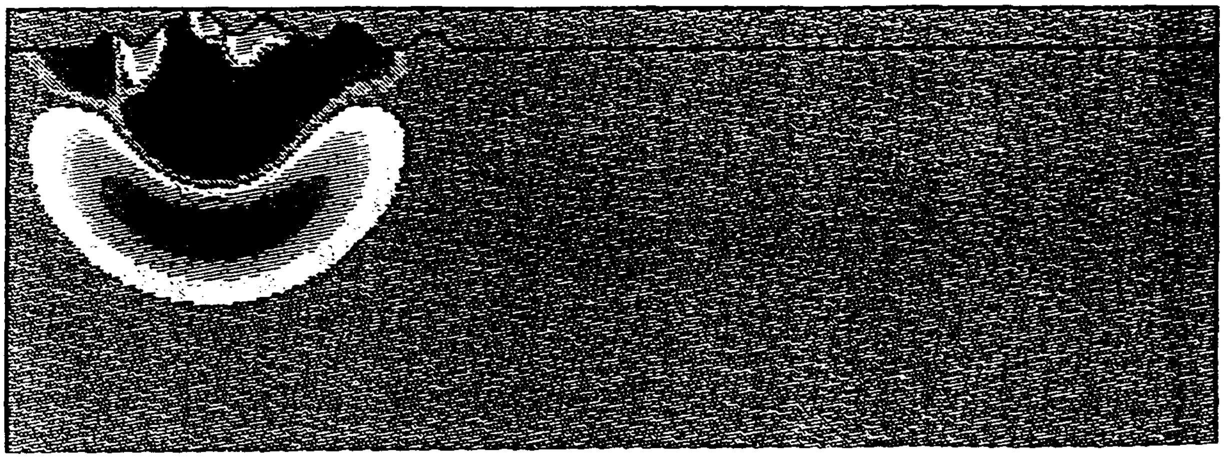

(b.) Vertical Velocity Field; .38 sec. after detonation

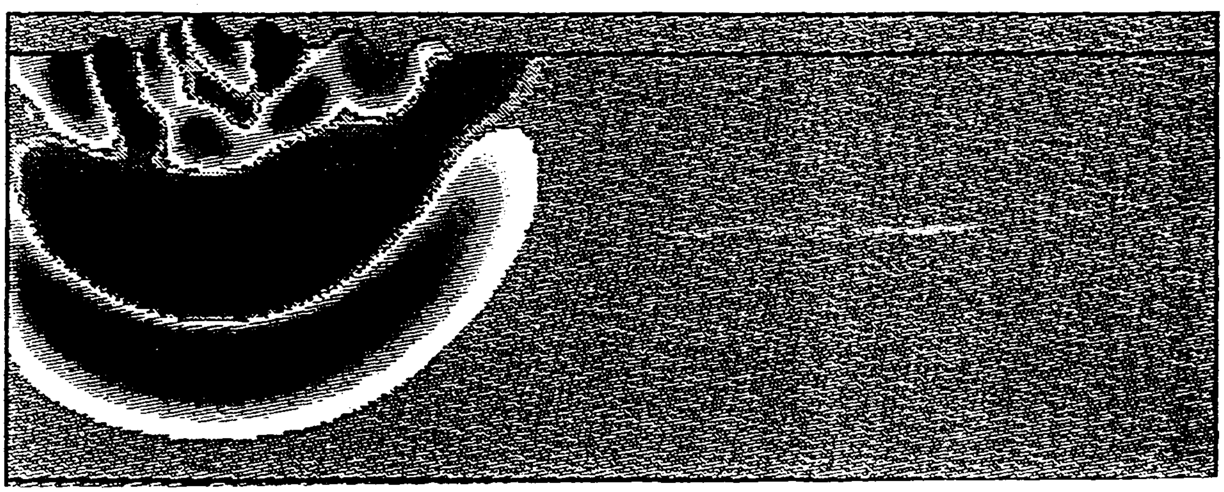

(c.) Vertical Velocity Field; .55 sec. after detonation

Figure 18-a. Contours of the vertical particle velocity from an explosion 300 meters below the free surface with high relief surface topography in the vicinity of the source area. The dimensions of the cross-section shown is 9 km. wide by 3.45 km. deep. Maximum surface elevation is 300 meters. Red denotes zones of a downward vertical velocity component, blue is an upward velocity

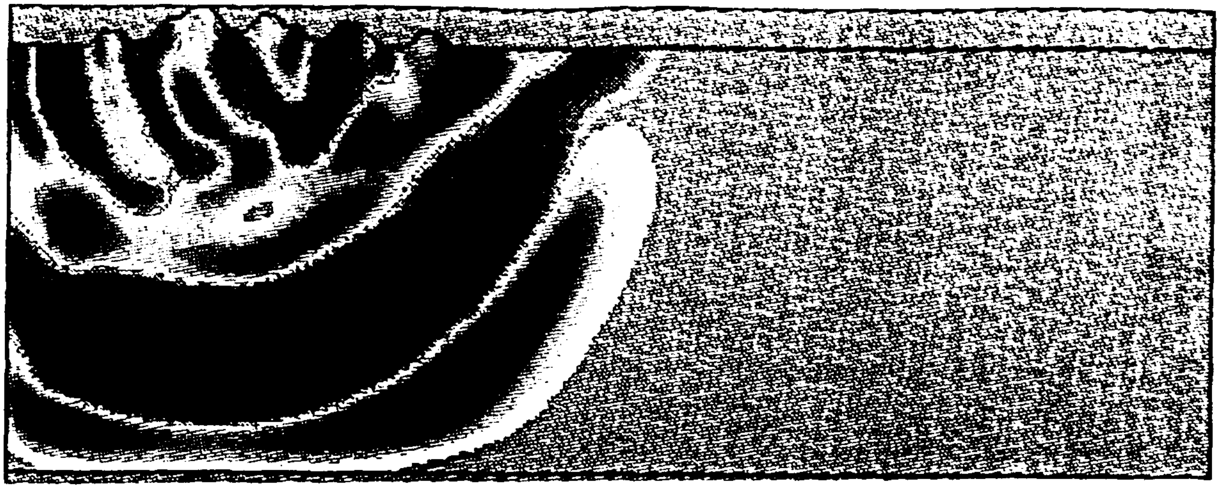

(d.) Vertical Velocity Field; .71 sec. after detonation

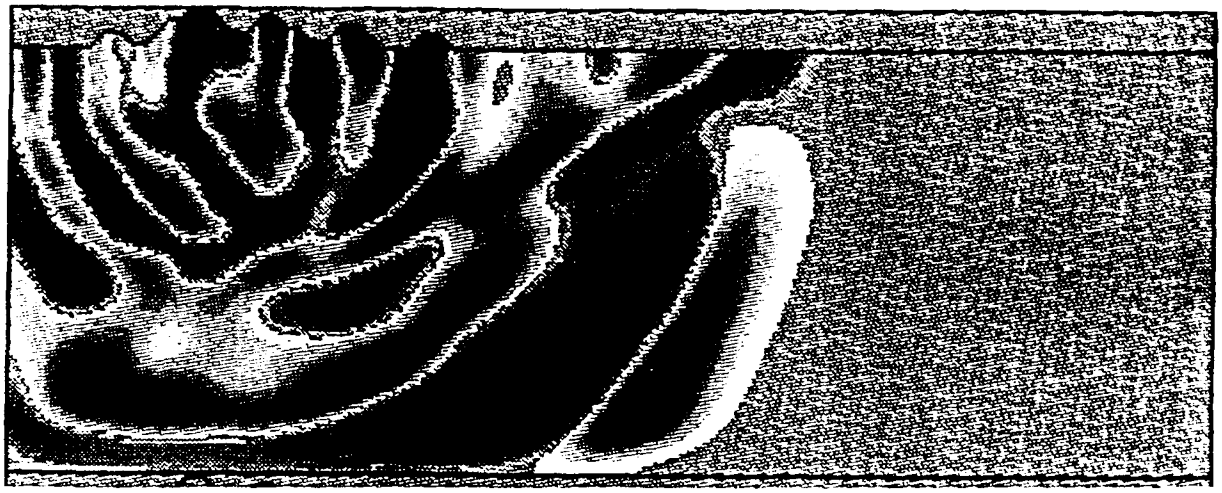

(e.) Vertical Velocity Field; .92 sec. after detonation

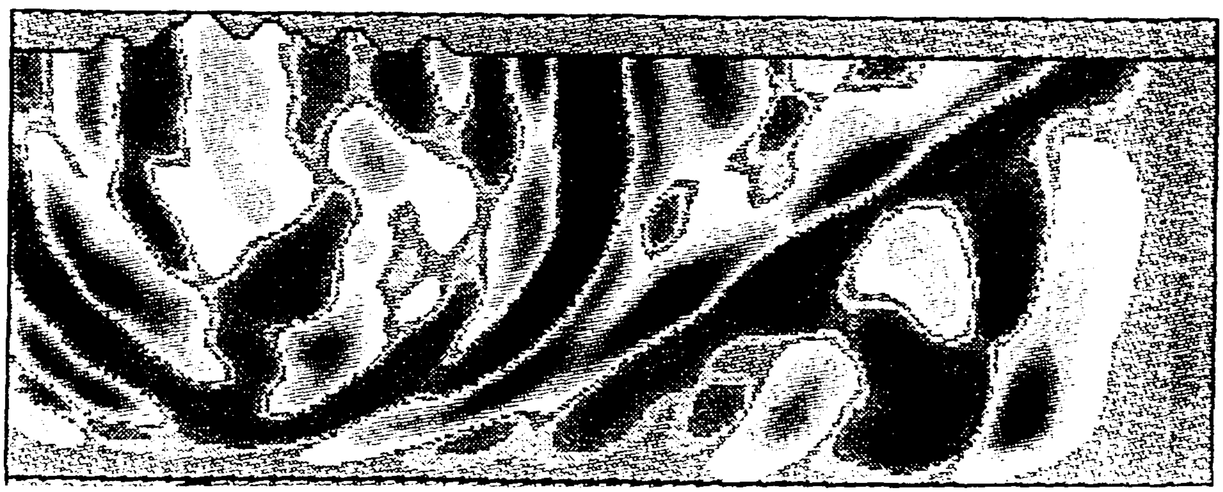

(f.) Vertical Velocity Field; 1.37 secs after detonation

Figure 18-b Contours of the vertical particle velocity from an explosion 300 meters below the free surface with high relief surface topography in the vicinity of the source area. The dimensions of the cross-section shown is 9 km wide by 3.45 km deep. Maximum surface elevation [illegible]. Red denotes zones of a downward vertical velocity component, blue is an upward velocity.

relief on the surface reflections following the direct P wave, for example, producing rather large variations in the P wave amplitudes as a function of emergence angle from the source area. These effects can also be seen in the time series recorded at the free surface at greater distance from the source zone. In this regard, Figure (19) shows recorded particle velocity at 6 km. from the source, under conditions in which the rough, near-source topography is either present (b. and d.) or absent (a. and c.). The effects of shallow fine scale layering are also indicated by these examples.

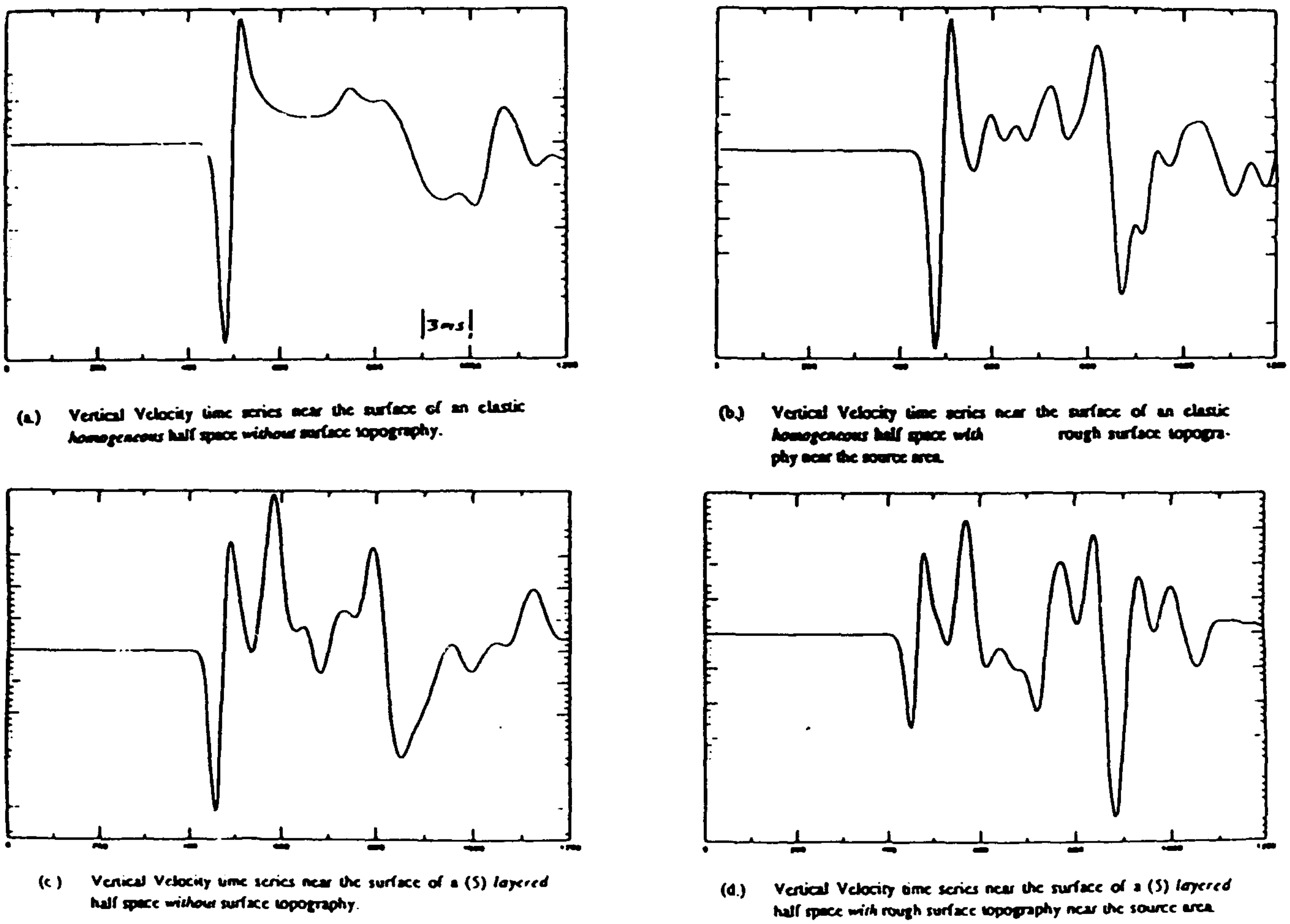

(a.) Vertical Velocity time series near the surface of an elastic *homogeneous* half space *without* surface topography.

(b.) Vertical Velocity time series near the surface of an elastic *homogeneous* half space *with* rough surface topography near the source area.

(c.) Vertical Velocity time series near the surface of a (5) *layered* half space *without* surface topography.

(d.) Vertical Velocity time series near the surface of a (5) *layered* half space *with* rough surface topography near the source area.

Figure 19. The effects of near source topography and fine scale layering on the wave field from a buried explosion source (300 m depth). Observations are at 6 km from the source on the free surface.

Clearly the examples show that complexities in the P and P_n coda, of the type observed, can be produced by topographic features and/or near source fine scale layering. In future studies we will systematically examine these effects, using realistic topography and structural layering and compare these results to observational data. In addition, using extended versions of the numerical modeling programs, whose out-put is illustrated here, we will include failure phenomena in the near source region to produce spallation, in order to evaluate its contribution to the radiated wave field.

The effects of strong and moderate lateral variations in near source shallow structure can, of course, also be included and can be systematically studied along with all the other medium characteristics producing strong perturbations in the wave field. Through this approach we hope to be able to "sort out" the quantitative nature of each of the effects on the directly radiated seismic field from explosions and be able to evaluate their total impact on source depth estimates, yield estimation and discrimination. As noted, the effects of strong "random" fluctuations in material properties at upper and mid-crustal depths is also of importance in producing scattering that can enhance P_g and L_g excitation, while reducing R_g by scattering losses with distance. Figure (20) shows our preliminary modeling tests using numerical simulations in 2-D models with randomized intrinsic velocities. Clearly, the complex forms of observed seismic data have a strong resemblance to the synthetics obtained in a randomized earth model. Of course our approach will be to systematically investigate this kind of scattering effect, particularly as a loss mechanism for R_g and as an excitation mechanism for L_g and P_g, while also carefully evaluating the "trade-off" of anelastic attenuation versus this scattering process for R_g, as well as the other possible/probable mechanisms of P_g and L_g excitation due to major lateral variations in structure.

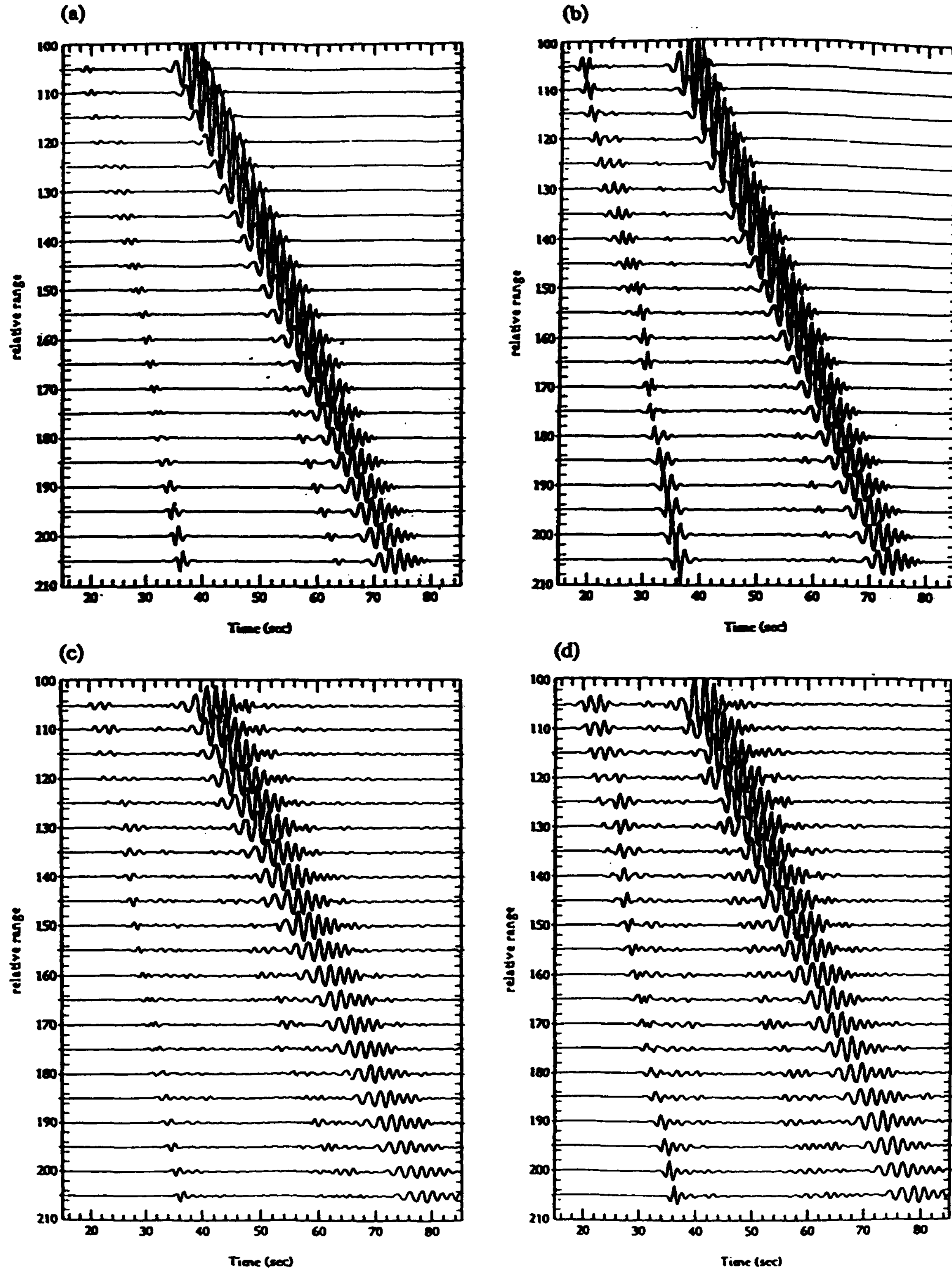

Figure 20. Effects of vertical elastic parameter randomization. Insets a. and b. are vertical and radial velocity components without radomization. Insets c. and d. are for the same structure with superimposed randomization of 25% at the surface to 10% at the base of the crust for the elastic velocity variation with depth.

In regard to the latter effects involving major structural discontinuities, Figure (21) shows examples of the effects of a major shallow structural transition, in this case a deep, low velocity, sedimentary basin within a higher velocity, largely igneous, crust. As illustrated, features of this type strongly affect high frequency surface waves, like R_g, and produce mode coupling effects that give rise to enhanced, and complicated, P_g and L_g excitation. We therefore will study such strong structure induced effects on a systematic basis to try to quantify the variability of discriminatory signals, like P_g and L_g, in order to assess what characteristics of these signals nevertheless remain robust and could be used for reliable discrimination under a variety of structural conditions.

Thus, with our present analytical modeling capabilities for both sources and wave propagation, in both vertically and laterally varying media, we expect to provide a means of predicting and understanding very complex source and near - source behavior (eg. multiple explosions in fractured media) as well as complexities in wave propagation effects.

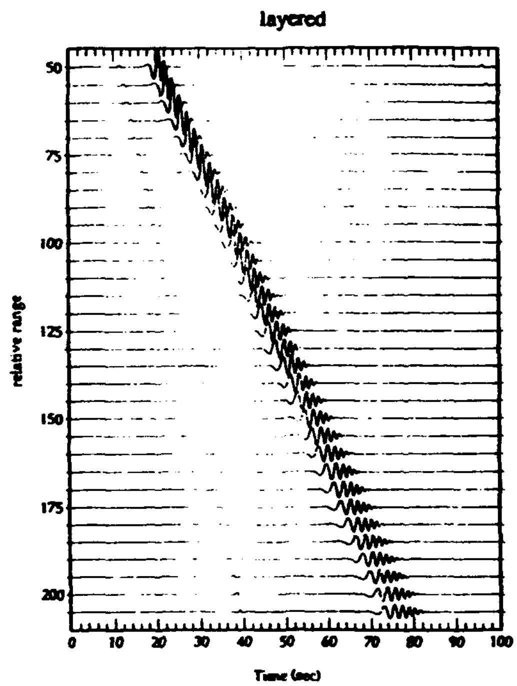

Figure 21-a. Pseudospectral synthetic seismograms for a layered earth structure. The explosion source was applied near the free surface with a maximum frequency content of 1 Hz.

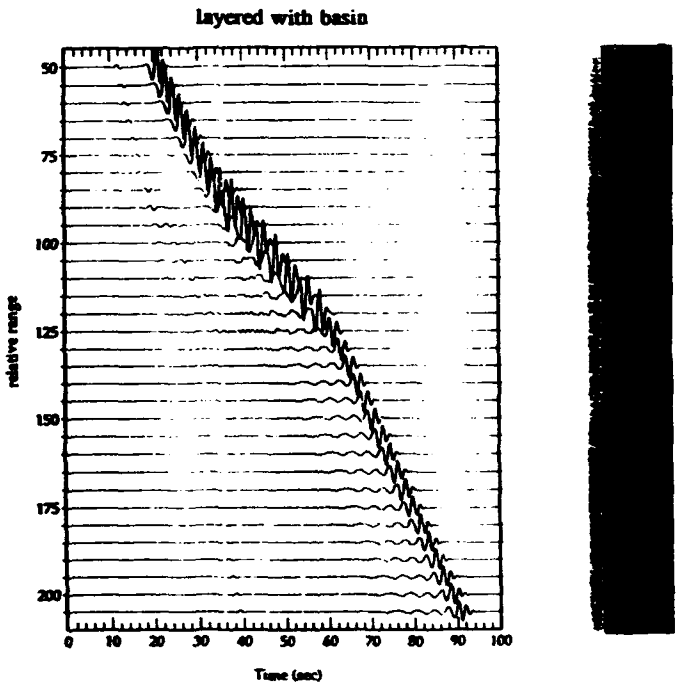

Figure 21-b. Pseudospectral synthetic seismograms for the layered earth structure used in 21-a but with the inclusion of a 3 km-deep low velocity sedimentary basin. A contour of the model's 2-D velocity structure is pictured on the right.

References

[1] C. Canuto, M. Y. Hussaini, A. Quarteroni, and T. A. Zang. *Spectral Methods in Fluid Dynamics.* Computational Physics. Springer Verlag, New York, 1988.

[2] C. Cerjan, D. Kosloff, R. Kosloff, and M. Reshef. A nonreflecting boundary condition for discrete acoustic and elastic wave equations. *Geophysics*, 50(4):705–708, April 1985.

[3] C. R. Daudt, L. W. Braile, R. L. Nowack, and C. S. Chiang. A comparison of finite-difference and fourier method calculations of synthetic seismograms. *Bull. Seism. Soc. Am.*, 79(4):1210–1230, August 1989.

[4] H. Emmerich and M. Korn. Incorporation of attenuation into time-domain computations of seismic wave fields. *Geophysics*, 52(9):1252–1264, September 1987.

[5] A. C. Eringen and E. S. Suhubi. *Elastodynamics*, volume 2. Academic Press, New York, 1975.

[6] B. Fornberg. The pseudospectral method: Comparisons with finite differences for the elastic wave equation. *Geophysics*, 52(4):483–501, April 1987.

[7] B. Fornberg. The pseudospectral method: Accurate representation of interfaces in elastic calculations. *Geophysics*, 53(5):625–637, May 1988.

[8] D. Gottlieb and S. A. Orszag. *Numerical Analysis of Spectral Methods.* Society for Industrial and Applied Mathematics, Philadelphia, 1977.

[9] D. Harvey. Seismogram synthesis using normal mode superposition: the locked mode approximation. *Geophys. J. R. astr. Soc.*, 66:37–61, 1981.

[10] D. Kosloff, A. Q. Filho, E. Tessmer, and A. Behle. Numerical solution of the acoustic and elastic wave equations by a new rapid expansion method. *Geophysical Prospecting*, 37:383–394, 1989.

[11] D. Kosloff, D. Kessler, A. Filho, E. Tessmer, A. Behle, and R. Strahilevitz. Solution of the equations of dynamic elasticity by a chebychev spectral method. *Geophysics*, 55:734–748, 1990.

[12] S. A. Orszag. Numerical simulation of incompressible flows within simple boundaries: I. galerkin (spectral) representations. *Stud. Appl. Math.*, 50:293–327, 1971.

[13] H. Tal-Ezer, D. Kosloff, and Z. Koren. An accurate scheme for seismic forward modelling. *Geophysical Prospecting*, 35:479–490, 1987.

[14] J. E. Vidale. Comment on a comparison of finite-difference and fourier method calculations of synthetic seismograms by c. r. daudt et al. *Bull. Seism. Soc. Am.*, 80(2):493–495, April 1990.

[15] D. C. Witte. *The Pseudospectral Method for Simulating Wave Propogation.* PhD thesis, Columbia University, 1989.

[16] D. C. Witte and P. G. Richards. The pseudospectral method for simulating wave propagation. *Computational Acoustics*, 3, 1990.

3. Modeling Atmospheric Wave Fields and Ionospheric Electron Density Variations Due to Near Surface Seismic Sources

3.1. Modeling of Atmospheric and Ionospheric Gravity Waves

Because of the exponential decrease of atmospheric density with height, buoyant pulsed gravity waves generated by surface or subsurface seismic sources can be of appreciable amplitude through out the atmosphere. Furthermore, above 100km in height, these flow transients affect the ionospheric EM fields through changes in the distribution of the charged particles. Accurate modeling estimates of seismically generated gravity waves and their effects in the ionosphere have not, to our knowledge, been investigated.

The basic equations governing motions of the neutral atmosphere are the conservation laws of mass, momentum and energy together with the ideal gas equation of state. The specific nonlinear continuum equations incorporate advective terms as well as the gravitational field, gas compressibility, viscosity effects and thermal conductivity. For electron motions in the ionosphere a first-order continuity equation is used which assumes that electrons move with the neutral atmosphere.

In our work to date, the set of partial differential equations for the atmosphere are converted to a corresponding set of finite difference equations in order to effect numerical integration in time and space. The non-linear terms are treated non-locally on the lattice for stability, effectively controlling, internally, the instabilities. In addition, random velocities and pressures are attributed to the inherent fine scale turbulence in the atmosphere and are incorporated in the modeling as are mean drift particle velocities. In particular, in order to account for the inherent turbulence in the atmosphere, the flow variables at a point are decomposed into a mean flow, governing winds, and a perturbed flow that incorporates turbulence. A new approach, designed to include turbulence, has been developed using random perturbations obtained from a random number generator which are input directly into the finite difference equations. Turbulence is also produced by a random distribution of temperature at the surface which produces thermal structures with upward and downward flows. Horizontal winds, impacting on a variable and random topography, also produce upward and downward motions which have a random stochastic character.

The set of finite difference equations are numerically integrated in time and space. Upwind differencing is used for first order spatial gradients with the advection velocity terms acting at the upwind point. However, if the velocity operates on its own velocity gradient, such non-linear terms are treated non-locally on the lattice for stability, effectively controlling internally any unstable growth.

There are at least three types of boundary important in this modeling. The air-ground surface is topographically complex with a turbulent boundary layer of the order of a few meters at the interface. At this boundary, vertical velocities are random both in time and at spatial locations. Because of the presence of the lower boundary layer above a complex topography, horizontal velocities are not taken as zero but incorporate winds and turbulence effects. The top atmospheric boundary is open with decreasing density. The topmost boundary should mimic the conditions for an open atmosphere with specific considerations for buoyancy and field gradients. We have examined various options including fixing velocities and densities and their gradients. However, we have adopted the general open flow boundary such as we also used for the artificial side boundaries. The side boundaries are artificial, due to grid restrictions, and must mimic open boundaries that allow free flow in either direction. We have adopted the more usual approach wherein the dependent variables are constrained to stay constant at these open boundaries.

3.2. Conservation Laws

The continuity equations are based on the values of the fields at particular points in space and time. Conservation of mass is expressed as,

$$\frac{\partial \rho}{\partial t} + \frac{\partial}{\partial x_j}(\rho u_j) = 0 \qquad (1.)$$

where ρ is density and u_j is velocity in the x_j direction. Conservation of momentum is similarly expressed as:

$$\rho\left[\frac{\partial u_i}{\partial t} + u_j \cdot \frac{\partial u_i}{\partial x_j}\right] = \rho X_i + \frac{\partial}{\partial x_j} \cdot P_{ij} \qquad (2.)$$

where X_i are external forces, P_{ij} is the generalized stress such that:

$$P_{ij} = -p \cdot \delta_{ij} + 2\mu \cdot e_{ij} - 2/3\mu \cdot \delta_{ij} \cdot e_{kk} \qquad (3.)$$

with $e_{ij} = 1/2\left[\frac{\partial u_i}{\partial x_j} + \frac{\partial u_j}{\partial x_i}\right]$ the strain rate and μ the viscosity. Conservation of energy is:

$$\rho \cdot \frac{\partial}{\partial t}(c_v\, T) + \rho u_j \cdot \frac{\partial}{\partial x_j}(c_v\, T) = \frac{\partial}{\partial x_j}\left[K\,\frac{\partial T}{\partial x_j}\right] - p \cdot \frac{\partial u_j}{\partial x_j} + \Phi \qquad (4.)$$

where T is temperature, c_v is specific heat at constant volume, K is thermal conductivity, and Φ is the viscous dissipation. Here:

$$\Phi = 2\mu e_{ij}^2 - 2/3 \cdot \mu(e_{jj})^2$$

The equation of state for the atmospheric gas is taken to be ideal, i.e.

$$P = \frac{k_B}{m} \cdot \rho \cdot T \qquad (5.)$$

where k_B is Boltzmann's constant and m is the mean molecular weight.

3.3. Normalized Equations

In the fundamental equations, (1) through (5), the dependent and independent variables can be normalized with respect to typical values. For an ambient atmosphere, with exponential decay of density with height, distances are normalized through the scale height, H, which, at the surface, is approximately 8400 metres. Velocities are normalized with respect to c_s, the sound velocity of air at the earth's surface. Similarly density, pressure and temperature are normalized to surface values, and the independent variable, time t, is normalized by (H/c_s). Thus for the continuity of mass, we get, as before,

$$\frac{\partial \rho}{\partial t} + \frac{\partial}{\partial x_j}(\rho u_j) = 0 \tag{6.}$$

where the new variables are now normalized and given the same symbol as the original variables. Incorporating gravity as the external force, the momentum conservation equation, (2), becomes

$$\rho \cdot \frac{\partial u_i}{\partial t} + \rho u_j \cdot \frac{\partial u_i}{\partial x_j} = - G_g \cdot g(z)\rho \cdot e_z - A_2 \cdot \frac{\partial P}{\partial x_i} + A_4 \cdot \Psi_i \tag{7.}$$

where $G_s = (g_s H/c_s^2)$ is a measure of the ratio of potential energy to thermal energy.

$A_2 = p_s/(\rho_s c_s^2)$ is a measure of the ratio of stress energy to thermal energy.

$A_4 = \mu_s/(\rho_s \cdot c_s)$ is the ratio of viscous to thermal energy.

Ψ is the normalized viscosity drag force,

$$\Psi_i = \frac{\partial}{\partial x_j}\left\{ \mu \left[\frac{\partial u_i}{\partial x_j} + \frac{\partial u_j}{\partial x_i} \right] - 2/3 \cdot \mu \cdot \frac{\partial u_k}{\partial x_k} \cdot \delta_{ij} \right\}$$

where μ is normalized to μ_s, the viscosity at the surface. In the atmosphere, μ is usually taken to be constant for the molecular viscosity. In the case of conservation of energy, the normalized equation is

$$\frac{\partial T}{\partial t} + u_j \cdot \frac{\partial T}{\partial x_j} = A_8 \cdot \frac{\partial^2 T}{\partial x_j^2} - A_6 \cdot \frac{\partial u_j}{\partial x_j} + A_5\, \Phi \tag{8.}$$

where

$$A_5 = \mu_s \cdot \frac{k_b}{m \cdot c_v} \cdot \frac{c_s}{(p_s \cdot H)} = A_6 \cdot \frac{A_4}{A_2}$$

$$A_6 = \frac{k_b}{m \cdot c_v}$$

$$A_8 = A_6 \cdot K \cdot \frac{T_s}{(p_s \cdot c_s \cdot H)}$$

where K is, as usual, taken constant for the atmosphere. The equation of state, on normalization, is

$$p = \rho \cdot T \cdot /m(z) \tag{9.}$$

where the ideal equation of state at the surface is $p_s = \frac{k_B}{m_s}\rho_s T_s$ with m_s the surface value of mean molecular weight (29.0) and m(z) the height-dependent normalized value.

3.4. Ionospheric Motions

The basic conservation law of charged particles, assuming no creation or annihilation, is:

$$\frac{\partial N_\alpha}{\partial t} = - \frac{\partial (N_\alpha \cdot u_{j\alpha})}{\partial x_j} \tag{10.}$$

where N_α is the number of particles of type α and $u_{j\alpha}$ is their velocity in the j'th direction. The initial concentration of the charged particles is taken to be time-independent, with only a vertical functional dependence, N(z), where the subscript α has been dropped for the type of particle. Assuming only small changes in this concentration, the dependence can be found from integrating eqn. (10) over the range t_0 to the present. To zeroth order, this concentration change becomes:

$$\delta N(z,t) = -\frac{\partial N(z)}{\partial z} \cdot \int_0^t u_z(t')dt' - N(z) \cdot \int_0^t \frac{\partial u_j(t')}{\partial x_j} dt' \qquad (11.)$$

The first term in (11) is the concentration change due to the displacement of the ionospheric layer, while the second term arises as a result of compression or rarefaction and is the predominant term when dealing with processes involving characteristic dimensions smaller than the width of the layer. The velocity of the charged particle is usually assumed to be identical with that of the neutral gas to zeroth order and this is the velocity that is used in the finite difference calculations for electron density changes.

The initial concentration of electrons is taken to be that of a Chapman distribution which has a maximum density at 345 km height and decreases rapidly below about 90 km with the functional dependence on height defined by:

$$N(z) = N_c \cdot \exp\left(\frac{1}{2}(1-\xi-e^{-\xi})\right) \qquad (12.)$$

Where $= (z-h_c)/H$, $h_c = 345$ km, $H = 65$ km and N_c is the normalizing value.

3.5. Finite Difference Scheme

The set of non-linear partial differential equations are converted to a corresponding set of finite difference equations for explicit computer integration in time and space. Upwind differencing is used for first order spatial gradients, with the advection velocity terms acting at the upwind point. However, if the velocity operates on its own velocity gradient, such non-linear terms are treated non-locally on the lattice for stability, effectively controlling internally any unstable velocity growth.

The updated variable is projected not from just the old dependent variable, a process that is inherently unstable, but from a distributed smoothed average of the variable at locations surrounding the specific spatial location. Such a smoothing method brings stability to the differencing scheme. However, the attendant numerical diffusion is minimized by not smoothing the density variable, which has only a small effect on stability. This approach also helps in stabilizing the integration at grid corners and boundaries. The second order derivatives in the viscosity and thermal conductivity terms are modeled by finite differences taken at the surrounding spatial locations.

In the explicit integration scheme, the updated flow velocities, temperature and density are obtained via their continuity equations while pressure is obtained from insertion of the updated density and temperature into the ideal gas equation.

3.6. Boundary Conditions

There are at least three types of boundaries important to the modeling of fluid flows. The air-ground surface is topographically complex with a turbulent boundary layer attached. The top atmospheric boundary is open to space with decreasing density. The side boundaries are artificial, due to grid restrictions, and must mimic open boundaries that allow free flow in either direction.

At the bottom boundary vertical velocity functions are input as sources of momenta at spatial locations. Otherwise, as usual, vertical velocities are taken to be zero at the bottom. Because of the presence of the lower boundary layer above a complex topography, horizontal velocities are not taken as zero but, instead, constant velocity and density gradients are assumed in the vertical direction. For subsurface sources only momentum inputs are considered at this bottom boundary. For sources at or above the surface, both momentum and pressure conditions must be applied, just as in atmospheric sources.

The top-most boundary should mimic the conditions for an open atmosphere with specific considerations for buoyancy and field gradients. We have examined various options including fixing velocities and densities and their gradients. However, we have adopted the general open flow boundary, much as we use for the artificial side boundaries. As usual, in order to preserve conservation relations, all normal gradients are set to zero at these open boundaries. However, this would not permit heat flow through the boundary. Therefore the second-order normal derivative of temperature is made constant.

3.7. Turbulence Effects

In order to account for the inherent turbulence in the atmosphere below the thermopause, the flow variables at a point can be decomposed into a mean flow and a perturbed turbulent flow. In the momentum equation, additional components are thus obtained for the generalized stress. These are mainly interaction terms between the mean and perturbed densities and velocities, termed the Reynold's stresses, which represent the interaction of the mean flow with the background turbulence. These extra stresses have been approximated by various phenomenological approaches. Boussinesq introduced the concept of eddy viscosities in order to use the Newtonian equations with the usual but much larger viscosity term. Our models evaluate the efficacy of this method using an eddy thermal conductivity. We also attempt to evaluate different forms of these Reynold's stresses through algorithmic modeling of various drag forces that mimic the effect of these interaction terms. It is found that even small drag forces of a particular type can alter the flows and their temporal dependence. An alternative approach to turbulence is developed in the use of random perturbations, obtained from a random number generator, and input directly into the finite difference equations.

3.8. Modeling Results

Explosive sources at and below the ground are simulated by computations in a solid continuum and their resultant effects on the atmosphere, at the solid-air interface, are integrated upward and outward. Various velocity sources are used at the lower boundary with differing time, amplitude and radial dependences. The standard input is a source, comprised of the first differential of a gaussian in time, that approximates the initial pulse from an underground explosion. Cartesian coordinates are used to model the 3-dimensional system, with the source at the center of the bottom plane.

Figure (22) shows results of modeling the low frequency gravity waves (or acoustic-gravity coupled waves) in the atmosphere and ionosphere due to a contained underground explosion just beneath the ground surface. The predicted electron density fluctuations, using equation (11.), are also shown in the upper left panel. These results show that the maximum of the disturbance is well behind the acoustic wave at the front which, for the instant of time shown here, is well above the 400 km. altitude and is also small relative to the amplitude of the fields indicated for this gravity controlled disturbance. Figures (23) and (24) show the disturbance at early and late times, whereas Figure (22) shows an intermediate time relative to these latter two "snap-shots" of the fields. Note that the late time disturbance is quite complex, with the velocity and temperature fields showing an oscillatory character as functions of altitude. (This is also true of the electron density but is not obvious from the color coded amplitude scale used for the figures.)

In Figure (23), which shows the disturbance at an early time, the true acoustic wave front is somewhat above 300 km, well above the large amplitude disturbance shown here, and as an amplitude lower than the first level of the coarse color table used and does not show up above the background color in the figure. In any case, the pure acoustic wave is small relative to the lower frequency, gravity controlled, disturbance shown here. Consequently, it is this strongly nonlinear disturbance that appears to be the best target for detection by

ELECTRON DENSITY PRESSURE TEMPERATURE

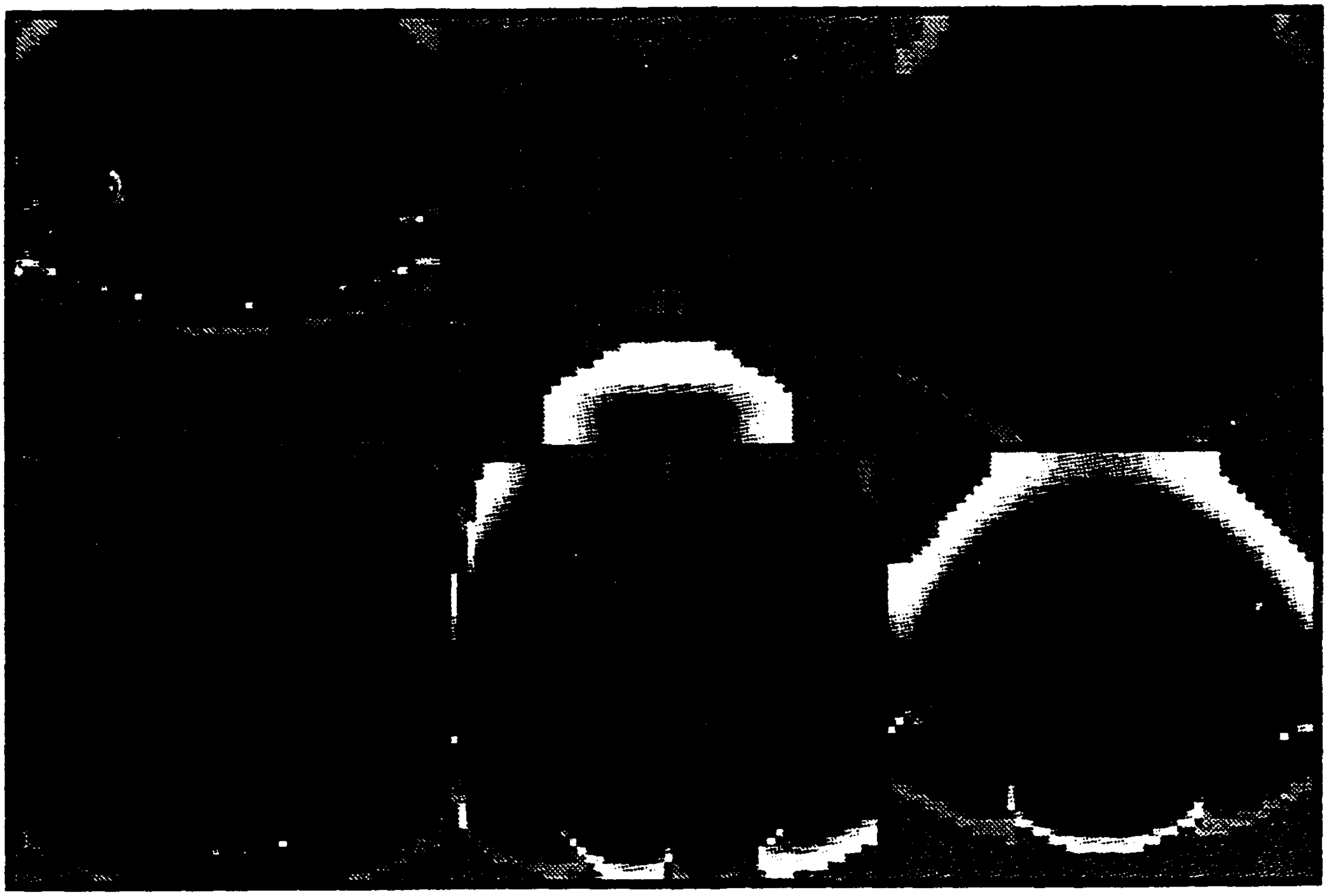

VERTICAL VELOCITY HORIZONTAL VELOCITY INWARD VELOCITY

Figure 22. CROSS-SECTIONS, height 400km width 800km, of spatial distributions of changes in atmospheric and ionospheric fields due to ground motions produced by a subsurface explosion. Acoustic-gravity waves propagate upward and outward in the ARDC standard atmosphere. Electrom density changes in a chapman model are due to the electrons following the motions of the predominant neutals. This pattern depicted occurs at a time of about 10 minutes after ground movement with onset of wave flipping at the 100 km region. Blue colors denote negative values with red denoting positive values.

EARLY TIMES

ELECTRON DENSITY PRESSURE TEMPERATURE

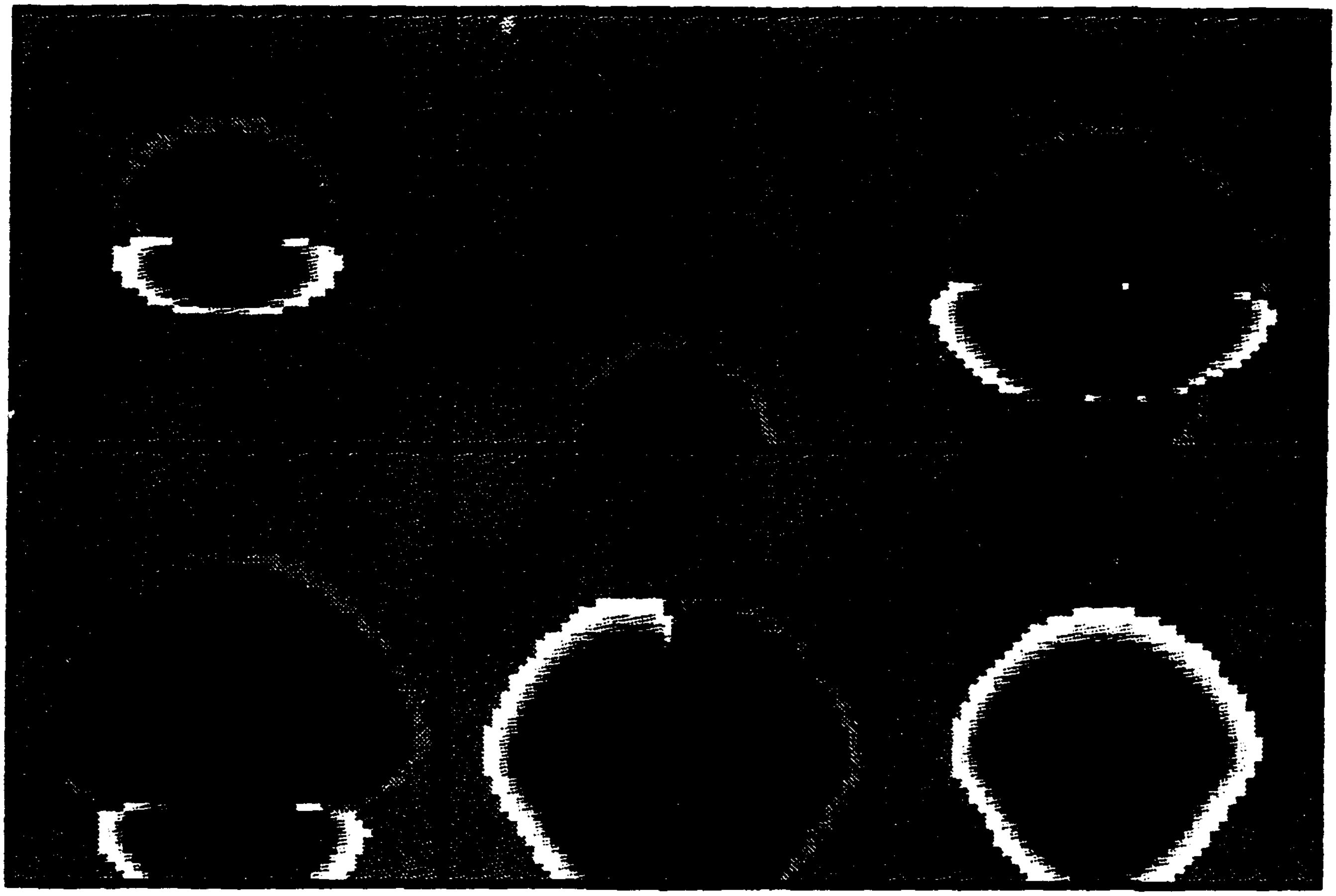

VERTICAL VELOCITY HORIZONTAL VELOCITY INWARD VELOCITY

Figure 23. CROSS-SECTIONS, height 400km, width 800km, of spatial distributions of changes in atmospheric and ionospheric fields due to ground motions produced by a synthetic subsurface explosion.

LATE TIMES

ELECTRON DENSITY PRESSURE TEMPERATURE

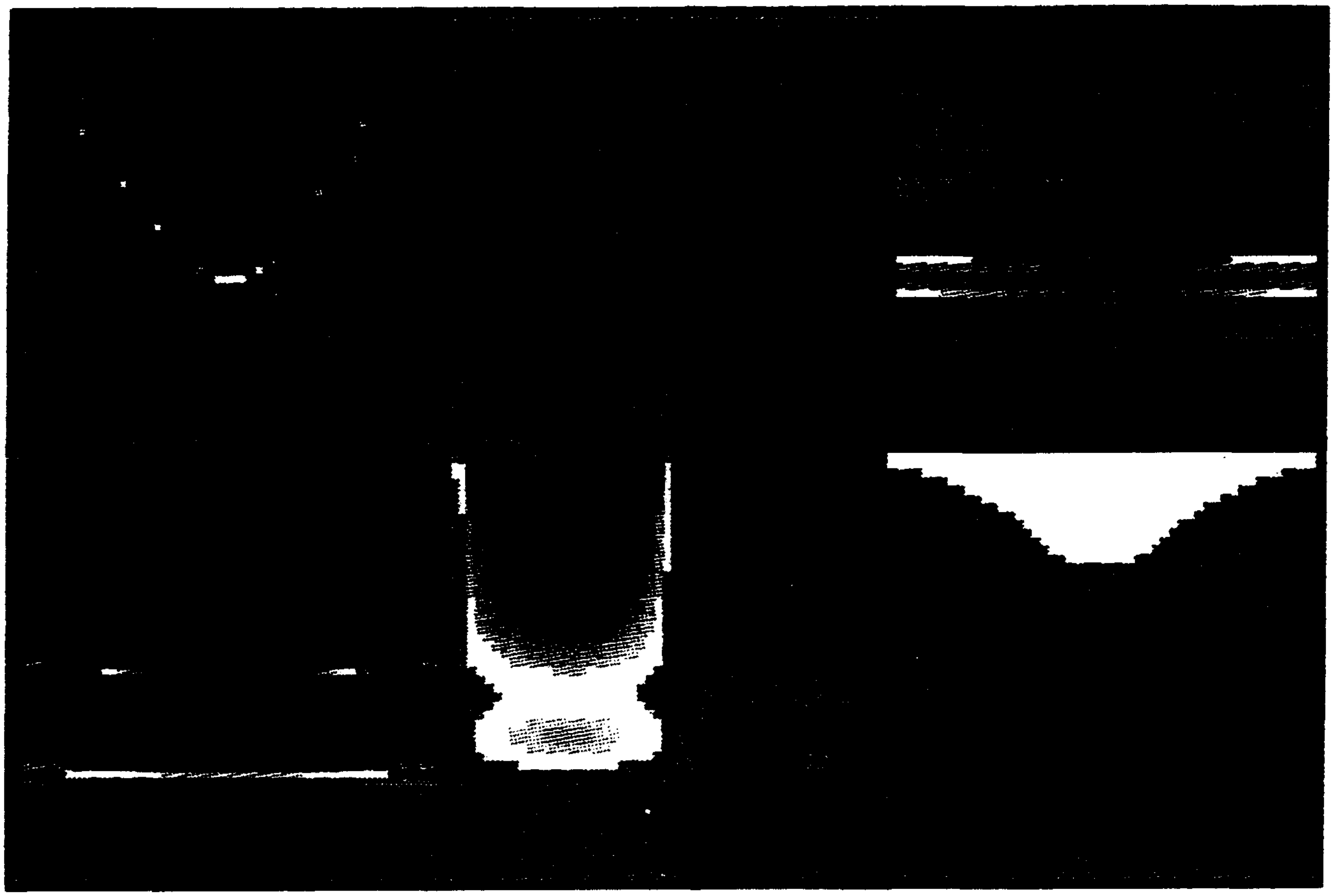

VERTICAL VELOCITY HORIZONTAL VELOCITY INWARD VELOCITY

Figure 24. CROSS-SECTIONS, height 400km, width 800km, of spatial distributions of changes in atmospheric and ionospheric fields due to ground motions produced by a synthetic subsurface explosion.

electromagnetic sounding methods since the associated electron density fluctuations are many time larger than those from the acoustic (or "shock") front.

A more detailed representation of the field variables (velocity and pressure) are shown in Figure (25). Here the fluctuating nature of the predicted disturbance is evident. The general predicted form of this disturbance, which is reflected in electron density variations, should allow this nonlinear wave to be easily detected by E-M sounding methods.

The results of the atmospheric modeling of the gravity wave effects from a surface explosion can be summarized as follows:

(1.) A time dependent transient pulse propagates upward with increasing amplitude relative to the ambient pressure. This produces asymmetric flows which control the flow development and the upward propagation of the transient. The initial positive density pulse is propagated upward more slowly than the following negative density pulse which has increased buoyancy. This initiates a sequence of circulation patterns that develops through what appears to be asymmetric triangular modes across the horizontal cross-section. The circulation patterns for the phenomena are characterized by upward central motions of the lighter matter, which, at the neutral buoyancy level, push outward to the side. The centroid of the transient pulse initially moves upward rapidly, but slows down to the group velocity speed of sound in the atmosphere. The advected air mass tries to remain in its horizontal stratification in order to minimize changes in its gravitational potential. However, it appears that energy and momenta are transported through traveling waves in the circulation pattern. Similar effects have been observed in the real atmosphere when thermals propagate upward from the Earth's surface with similar circulation patterns.

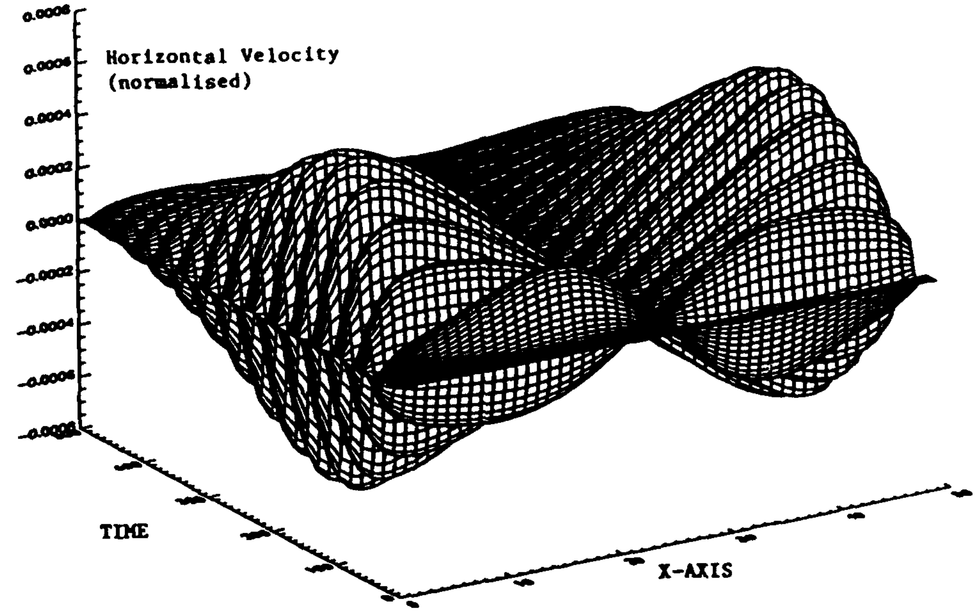

Figure 25 a,b. Horizontal velocity and Pressure, respectively, as a function of time along the x axis at an altitude of 170 km.

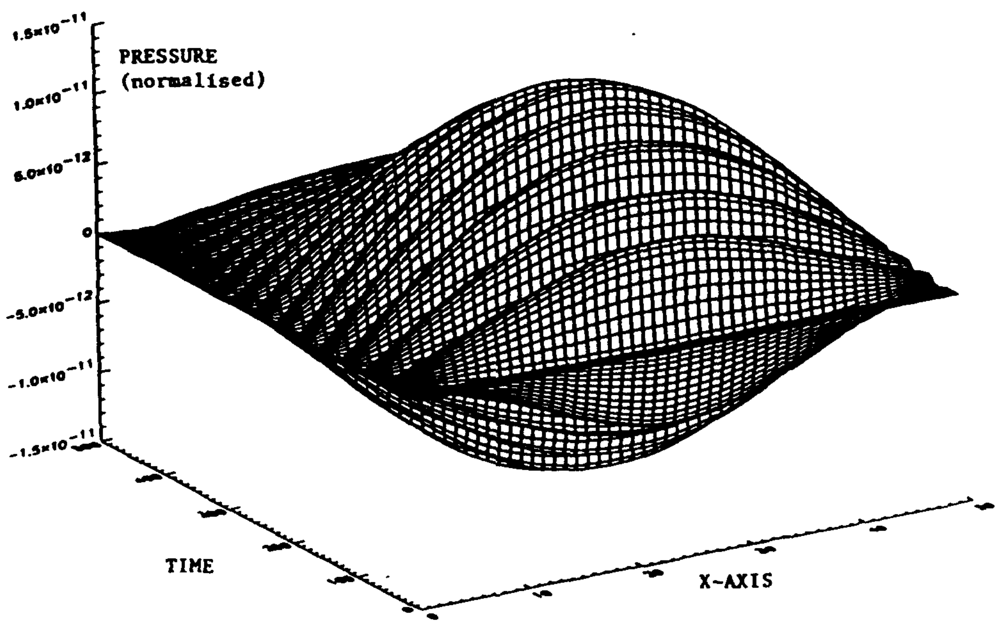

(2.) After a model dependent characteristic time, a bifurcation of the flow occurs with the eventual reversal of the velocity directions. The bifurcation phenomena occurs in this model, every 100 seconds, so that it has a period of just over 3 minutes. A drag force is input in order to model the effect of the inherent background turbulence of the atmosphere. A drag force, which removes 2% of the component velocities at each computational grid point at each time step, removes the periodic bifurcation and a standing wave is formed in the atmosphere with constant field patterns. However, with a 1% removal rate, the patterns are periodic with similar bifurcations as in the zero drag case. Because existing atmospheric turbulence acts on the transient gravity wave as a perturbation, we have also modeled its effect by imposing a random component on each field at each time step and grid point. The usual bifurcations are obtained but with differing patterns from the zero turbulence case. However, the appearance of the pressure and density fields is more realistic due to added diffusion and random components.

As the transient pulse moves upward in the atmosphere, it magnifies in amplitude relative to the exponentially decreasing ambient pressure. Thus, the level at which a specific pressure is located will oscillate as the transient pressure pulse moves through. To the first order, the electrons in the ionosphere are assumed to move with the flow of the dominant neutrals. Thus the change in the electron density can be calculated from a conservation law, whose integration in time gives the total electron density variation. The ambient electron density is approximated by the Chapman function which has a maximum electron density at 350 km and effectively zero electron density below about 90km. For reasonable velocity sources at the ground surface, we find that changes in electron density from 100 km and upward are at least of the same order as those observed by EM experiments conducted over surface and subsurface explosions, and generally for the gravity wave disturbance it appears to be larger. In this

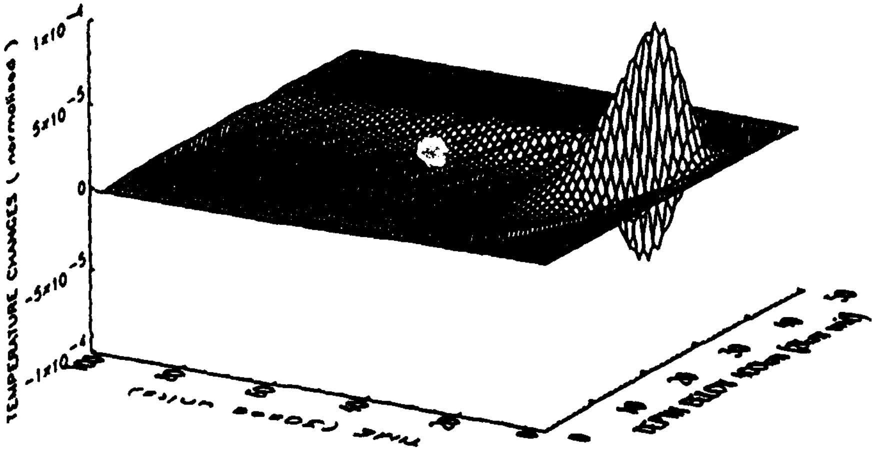

(a.) Time and spatial variation of the temperature change expressed as a fractional change in the temperature.

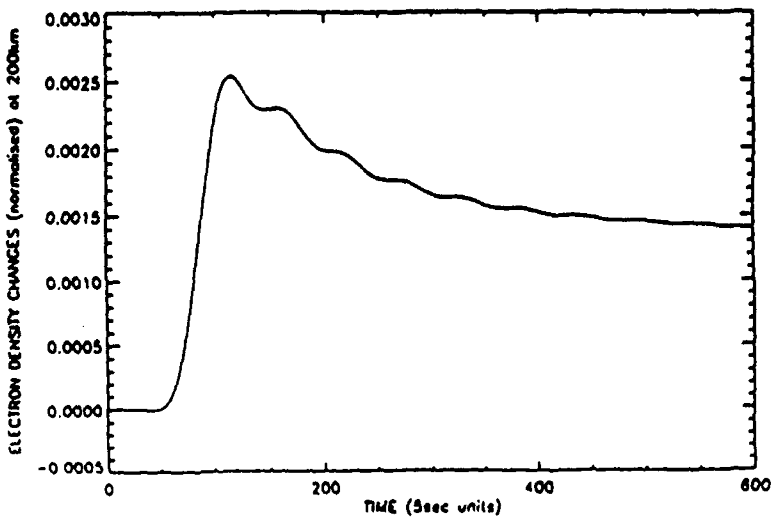

(b.) Time variation of the electron density change expressed as a fractional change in the electron density at 200 km. altitude.

Figure 26. Fluctuation in the ionospheric temperature and electron density due to a transient pressure pulse at the earth's surface form a contained near surface explosion. The source is at 300 m below the surface and the peak surface particle velcity is near 3 m/sec., the peak acceleration is 1.2 g and the event body wave magnitude (mb) is near 5. (Archambeau, et. al., 1992)

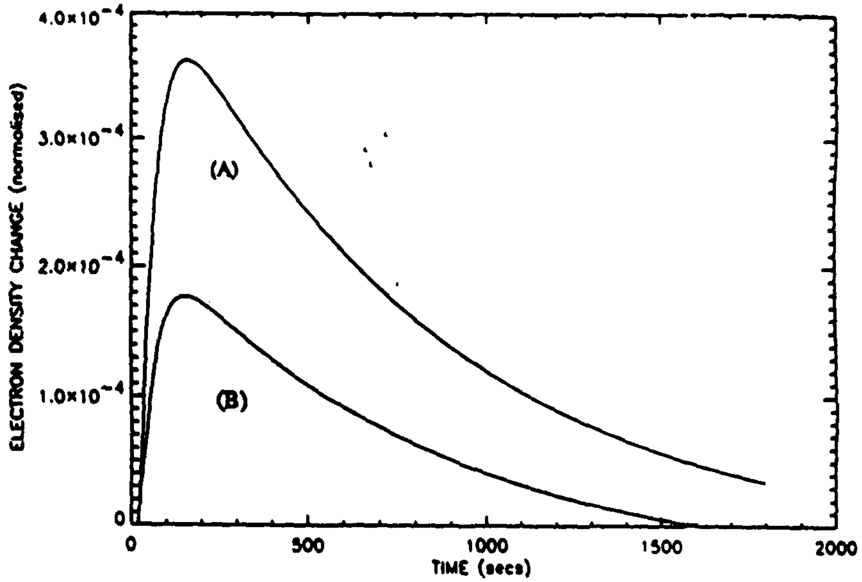

Figure 27. Normalized electron density changes at at height of 1.50 km above a surface vertical velocity sources, comprised of a bipolar pulse with a duration of 1 sec.;
(A) source has maximum velocity of 3 m/sec;
(B) source has maximum velocity of 1.5 m/sec. and the actual electron density change is 10 times the plotted value.

regard, Figure (26) shows an example of the predicted gravity wave induced fluctuations in temperature and electron density in the ionosphere due to a near surface underground explosion. In this case the explosion was taken to be a tamped underground nuclear test at a depth of 300 meters with a seismic body wave magnitude near 5. (Much smaller industrial explosions, very near or at the earth's surface , would typically produce comparable or even larger signals). Figure (27) shows electron density fluctuations for other source pressure histories and indicates the sensitivity of the perturbation form to source character.

4. Modeling High Frequency Seismic Noise: Atmospheric Sources

The nature of high frequency seismic noise is indicated by the observed noise acceleration power shown in Figure (28). The station shown (BAY) is near the former Soviet test site in Kazakh and is typical of the high frequency noise seen both within the former USSR and elsewhere. Three components of ground acceleration on the surface and at about 100 meters depth are shown. Both high and low wind level seismic noise spectra are shown on each plot. In all cases the high frequency seismic noise increases with high wind levels. It is also apparent that the acceleration power is roughly constant over the band from about 1 Hz to 30 Hz. Above 30 Hz the noise acceleration power decreases with increasing frequency, particularly in the bore-hole at 100m. depth.

Given the rather strong dependence of the noise level on wind velocity, it is natural to infer that atmospheric coupling at the earths surface is an important means of excitation of high frequency seismic noise. A more detailed understanding of the atmospheric excitation of seismic noise is clearly important since the reduction or cancellation of this noise is dependent on an understanding of its origins, mode of excitation and propagation within the medium.

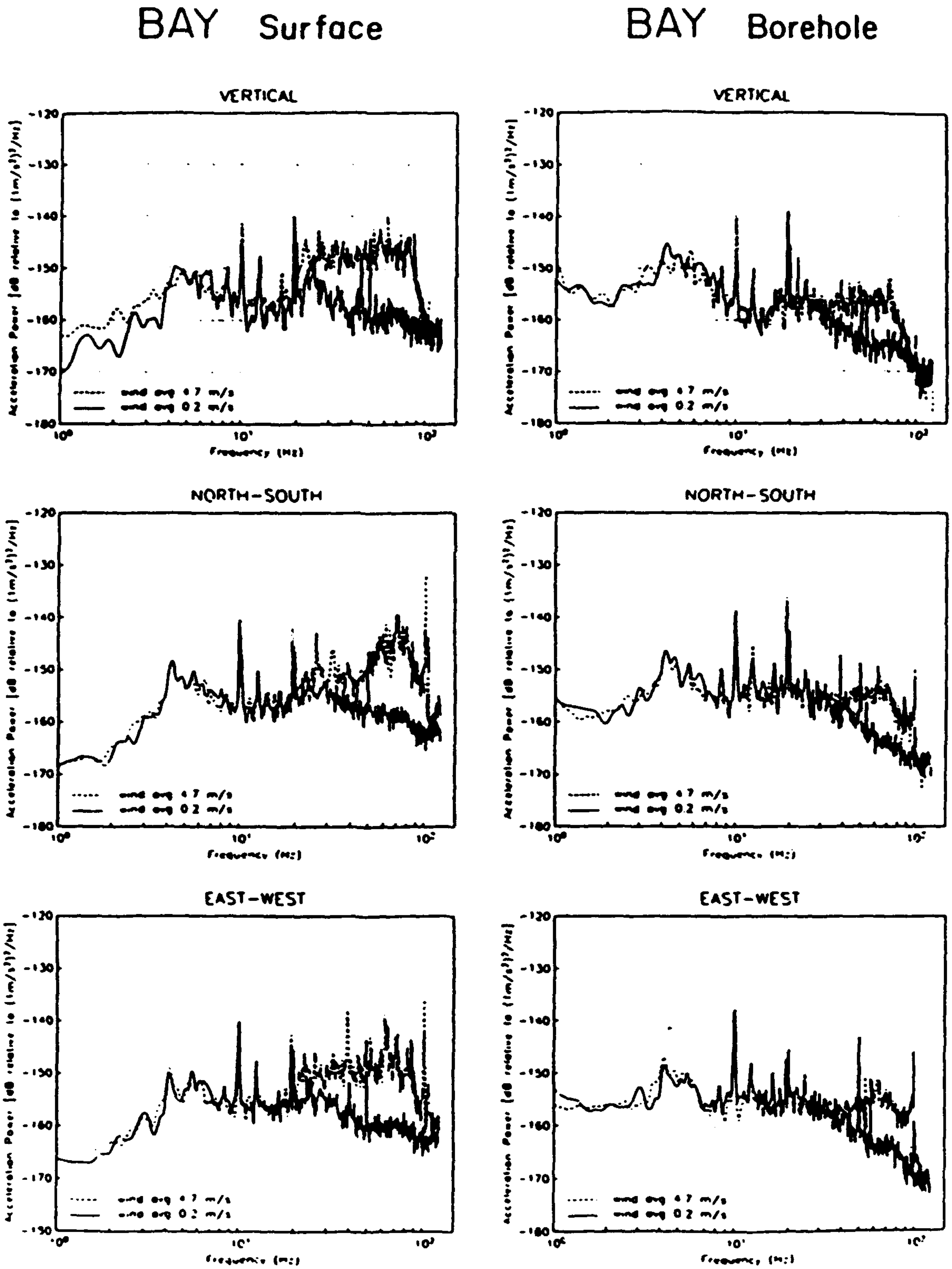

Figure 28. Observed high frequency seismic noise acceleration power spectra at a site near the test site in Kazakh. Two wind level conditions are shown for sensors at the surface and at a depth of about 100m. (Data from Berger *et. al.*, 1989).

In order to investigate the production of seismic noise by atmospheric processes, the atmospheric modeling programs were linked with the linear elastic seismic modeling programs. The lower atmosphere, composed of a day-time turbulence boundary layer with a heigh of 2 km, is simulated with a random surface topography. Winds, blowing on the topography, induce upward and downward flow velocities. Random temperature changes in space on the ground surface also produce flows that self-organize into plumes that coalesce above the boundary layer into larger scale thermals. Together with random turbulence in the boundary layer, these flows induce pressure and velocity fluctuations along the ground surface. These effects are the input into the seismic modeling code which integrates in time from the top-most surface boundary.

Figure (29) shows results of modeling atmospheric variations in pressure and velocity due to turbulence (top row) and induced seismic effects at depth produced by these atmospheric effects at a particular time (bottom row). An interesting feature of the seismic noise, produced by the essentially random fluctuations in the atmosphere, is its relative organization into spatial zones of coherent compression or dilatation (for example) at a particular time. This self-organization of the seismic noise field into coherent spatial zones in response to random atmospheric excitation is characteristic of the results of this modeling and suggests approaches to high frequency noise minimization using arrays that take advantage of these patterns.

Preliminary results indicate that the seismic noise that is produced decreases in amplitude with depth and, as shown in Figure (30), produces a seismic velocity spectrum that has a trend that decreases as 1/f with increasing frequency, in the range from about 1 to 50Hz. Below about 40 meters the seismic noise appears to interact in such a manner that much

SEISMIC NOISE FIELDS DUE TO ATMOSPHERIC TURBULENCE EFFECTS

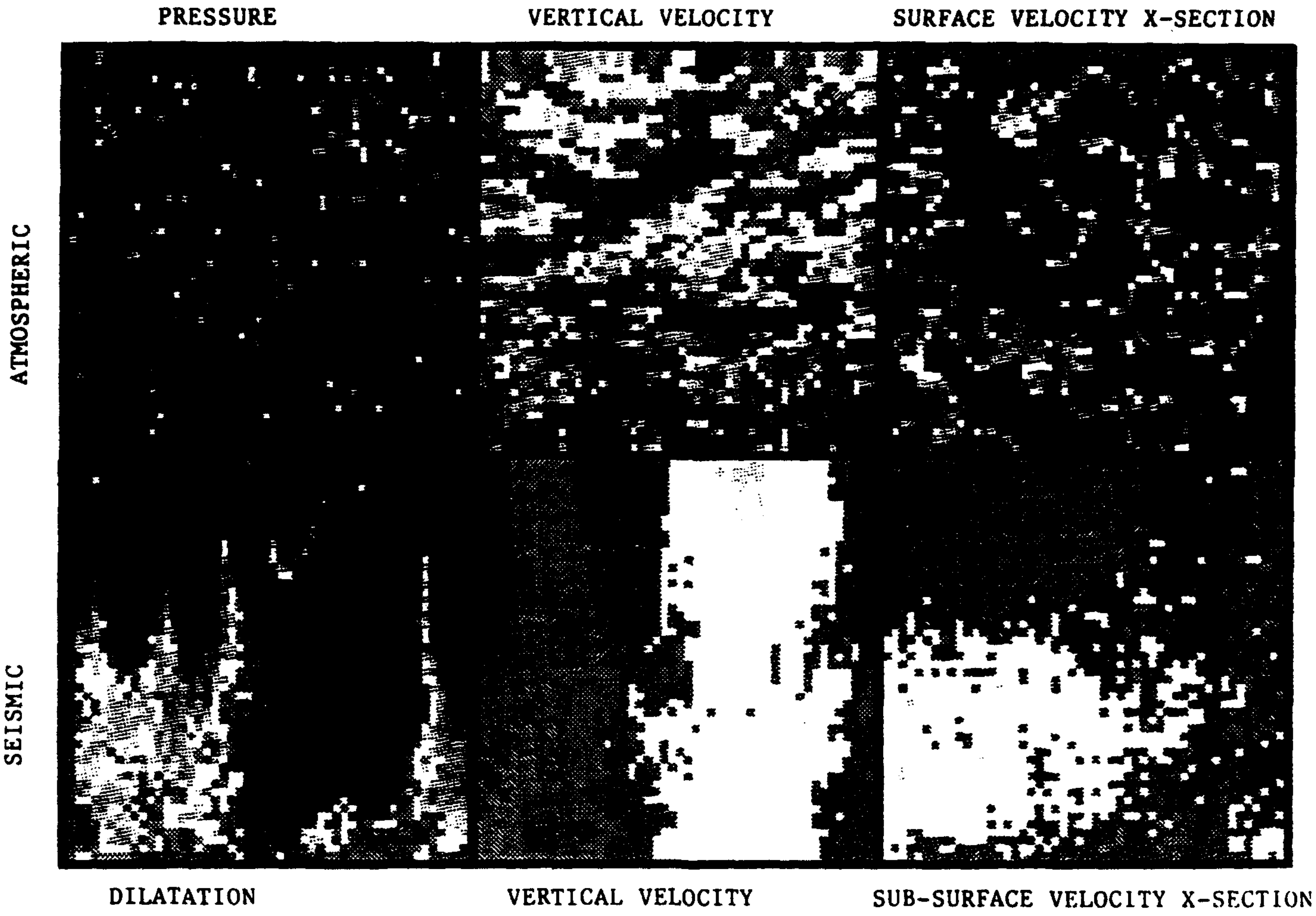

Figure 29. CROSS-SECTIONS, 50km by 50km, of atmospheric and seismic fields due to atmospheric turbulence generated by random temperature perturbations decaying inversely with height and possessing a uniform random distribution. Blue colors denote negative values with red denoting positive values. The four cross-sections on the left are height vertical and width horizontal; the two cross-sections on the right are width and breadth.

smoother variations in spatial distributions are obtained than at the surface and with associated decreasing fluctuations in time. Both topography and winds are found to be of major importance in terms of amplitude and character of the noise. From preliminary results it can be expected that time of day will also be important due to the change of the turbulent boundary layer with the heating of the Sun and its temporal dependence.

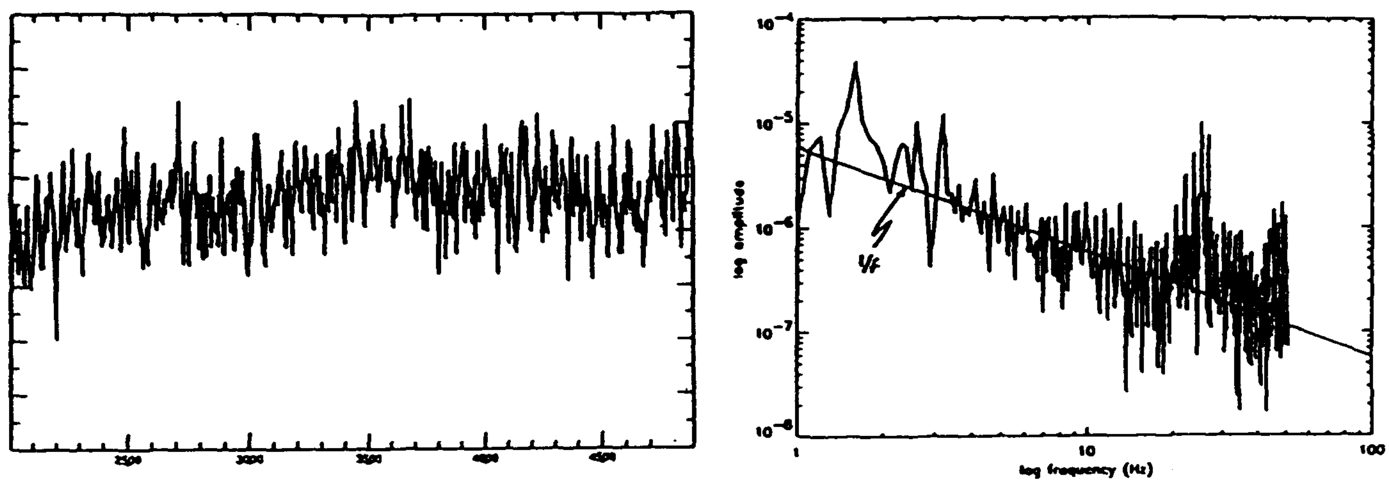

(a.) Seismic noise (velocity versus time) near the free surface due to the atmospheric turbulence.

(b.) Fourier spectrum of the seismic (velocity) noise in (a.). The trend of the mean spectrum is as f^{-1}, which is what is commonly observed.

Figure 30. Theoretically predicted seismic noise due to models of atmospheric turbulence at the earth's free surface.

Comparison of the modeling results in Figure (30) with the observations in Figure (28) shows that the velocity predictions are in agreement with the observations in that both, in the mean, show particle velocity decrease as 1/f with increasing frequency above about 5 Hz. This strongly implies that atmospheric sources (turbulence) is the major source of high frequency seismic noise.

5. Summary and Conclusions

Since the atmosphere is just another layer of the planet and wave phenomena in this region is coupled to that in the solid layers, and is of a form that is only modified from that of seismic waves by the differences in material properties and a different approximation of the same equations of motion, it seems evident that the boundary between the atmosphere and the lithosphere should not constitute a barrier to investigation or utilization of signal information. To ignore the atmosphere is to neglect an important source of data bearing on present monitoring problems.

In addition, it might be pointed out that sensing of atmospheric/ionospheric disturbances by electromagnetic sounding methods is only utilization of a particular sensing system and can be considered to be like the use of a seismic transducer to record near surface ground motion. Therefore, differences in the proposed study of atmospheric waves for monitoring and seismic monitoring research are not as great as might, at first, be thought.

The potential benefits of joint seismic/atmospheric monitoring are numerous. Direct recording of acoustic or gravity waves at surface stations provides another means of locating a source. Of most importance, however, is that merely recording such signals above noise levels indicates a shallow explosive source and not a decoupled nuclear test. Likewise the indirect EM sensing of the much larger ionospheric wave disturbances due to acoustic and/or gravity waves should be diagnostic of source depth simply by the inferred size of the signal, where surface or very near surface industrial explosions (of any type) will produce much larger signals than an earthquake or a tamped or decoupled nuclear test of comparable size. Naturally, deeper earthquakes, that can sometimes be confused with nuclear tests because of lack of good seismic estimates of depth, will produce no atmospheric effects while a shallow nuclear test should produce a moderate to small (but detectable) signal.

Therefore, the EM detected ionospheric waves could be very useful in rapidly identifying industrial explosions and isolating (by elimination) potential decoupled or tamped nuclear tests out of a group of seismically determined shallow events with explosion-like characteristics. Further, unrecognized deeper earthquakes could probably be eliminated as potential explosions because of the lack of a detectable ionospheric disturbance, although careful modeling of seismic source types at various depth locations will be required before this could be applied with confidence.

It therefore appears that by placing radio frequency receivers and transmitters in a distributed network, comparable to an in-country seismic monitoring network of about 30 stations, should make it possible to provide complete atmospheric monitoring capability on a continental scale. In principal it should be possible to identify large industrial explosions, with high probability, due to the strong EM signal shifts observed and thereby allow combined seismic and atmospheric monitoring to identify low yield coupled and decoupled nuclear tests in a background of industrial explosions and earthquakes.

We have tested and modified atmospheric modeling capabilities to include the most important non-linear effects, in particular the effects of sub-grid scale turbulence. We have made good progress on the turbulence phenomena by introducing a randomly fluctuating component to the field variables (i.e., pressure, velocities, temperature and density) that simulates sub-grid level turbulent effects. Results are encouraging and in particular give stable dynamical solutions to test problems that are comparable to observations.

The seismic investigations have focused on generation and testing of 2 and 3D finite difference programs that incorporate surface topography, medium randomness and lateral variability. Adaptation of FFT methods coupled with moving grids have been successful when tested against analytical and conventional finite difference methods and can, in principle, provide capabilities for predictions of wave fields in heterogeneous media at regional distance ranges using moderate sized computers (e.g., high level work-stations such as the Stellar Computer) with only modest core size requirements (i.e., a few hundred megabytes). Transmitting grid boundaries have also been developed and tested with success. Analytical (modal) theory methods are being developed for 3D laterally varying media, to be used along with the 2D theory already developed.

Results of modeling studies and their comparisons with observed data have shown that:

(1) The atmospheric-ionospheric modeling predictions of electron density fluctuations from the non-linear "gravity wave" have large amplitudes and wave forms of distinctive form suggesting easy detection by EM sounding methods.

(2) Coupled atmospheric-seismic modeling indicates that atmospheric turbulence, simulated by random fluctuations in state variables near the free surface, produces high frequency seismic noise with spectral character close to that observed; that is with a velocity amplitude spectrum varying as $1/f$ as a function of frequency above 1Hz.

(3) Seismic wave field modeling in complex structural models, incorporating rough, near source topography and fine scale randomized layering, produces seismic synthetics having the complex character of observed seismograms. Simple vertical and horizontal randomization can only be an adequate representation of earth structure, and the seismic wave fields observed, within a few tens of wavelengths from the source. Beyond that distance the effects of strong shallow lateral variations in both average and random characteristics of the earth's structure produce effects in the observed wave field that

become of first order and therefore important, so that accounting for large scale lateral variations is necessary to explain observed seismic wave fields in the regional distance range.

(4) Preliminary studies of particular complex seismic wave types, such as L_g and R_g, indicate that only large scale lateral variations in structure, in combination with both vertical and lateral randomization can explain the wave forms and attenuation characteristics observed.

6. References

Archambeau, C.B., Wave Propagation in Laterally Varying Media: A Mode Expansion Method, Submitted Geophy. Journal International, Roy. Astron. Soc., April, 1993.

Archambeau, C.B., J.B. Davies, and J.L. Orrey, Investigations of Joint Seismic and Electromagnetic Methods for Nuclear Test Monitoring, 1992, PL-TR-92-2158, ADA258597

Baker, D.M. and K. Davies, Waves in the Ionosphere Produced by Nuclear Explosions, *J. Geophys. Res., 73,* 448-451, 1968.

Berger, J., H.K. Given, F.L. Vernon, I.L. Nersesov, M.B. Gokhberg, O.A. Stolyrov and N.T. Tarasov, Studies of High-Frequency Noise in Eastern Kazakhstan, *Bull. Seism. Soc. Am.,* 1989.

Beynon, W.J.G. and E.S.O. Jones, Ionospheric Effects of Nuclear Explosions, *Nature,196,* 253-254, 1962.

Blanc, E., Neutral temperature and electron-density measurements in the lower E region by vertical HF sounding in the presence of an acoustic wave, *J. Geophys. Res.*, 87, 450-453, 1982.

Blanc, E., Interaction of an acoustic wave of artificial origin with the ionosphere as observed by vertical HF sounding at total reflection level, *Radio Sci.*, 19, 653-664, 1984.

Blanc, E., Observations in the Upper Atmosphere of Infrasonic Waves from Natural or Artificial Sources: A Summary, *Annales Geophysicae, 3,6 673-688.*

Blanc, E, and D. Rickel, Nonlinear Wave Fronts and Ionospheric Irregularities Observed by HF Sounding Over a Powerful Acoustic Source, *Radio Science, 24,3,* 279-288, 1989.

Canuto, C., M.Y. Hussaini, A. Quarteroni, and T.A. Zang. *Spectral Methods in Fluid Dynamics.* Computational Physics. Stringer Verlag, New York, 1988.

Carcione, J., D. Kosloff, A. Behle, and G. Seriani. A spectral scheme for wave propagation simulation in 3-D elastic-anisotropic media. *Geophysics, 57(12):1593-1607, December 1992.*

Davies, K. and D.M. Baker, Ionospheric Effects Observed Around the Time of the Alaskan Earthquake of March 28, 1964, *J. Geophys. Res., 70,* 2251-2254, 1965.

Deardorff, J.W., Sub-Grid-Scale Turbulence Modeling, *Advances in Geophysics, 28,* 337-344, 1985.

Dilts, G., *Dynamical Equilbrium: A Mathematical Model for the Dynamical Description of the Permanent Deformation of an Elastic Material Caused by Microfracture or Plastic Flow,* Ph.D. Thesis, Dept. of Physics, University of Colorado, 1985.

Evernden, J.R., C.B. Archambeau and E. Cranswick, An Evaluation of Seismic Decoupling and Underground Nuclear Test Monitoring Using High Frequency Seismic Data, *Rev. of Geophys.* 24, May 1986.

Fitzgerald, T.J. and R.C. Carlos - The effects of 450 kg. surface explosions at the E layer of the ionosphere, Preprint, Los Alamos National Lab., Oct. 1992.

Francis, S.H., Global Propagation of Atmospheric Gravity Waves: A Review, *J. Atmos. Terr. Phys., 37,* 1011-1054, 1975.

Friedmann, J.P., Propagation of Internal Gravity Waves in a Thermally Stratified Atmosphere, *J. Geophys. Res., 71,* 1033-1054, 1966.

Georges, T.M., Short-period ionospheric Oscillations associated with Severe Weather, in Acoustic Gravity Waves in the Atmosphere, 171-178, (ed. by T.M. Georges), E.S.S.A. Symposium, U.S. Govt. Printing Office, Washington, D.C., 1968.

Gokhberg, M.B. *et. al.,* Electromagnetic Effects of Nuclear Underground Explosions and Possibilities of Non-seismic Verification Methods, Internal Report, Institute of Physics of the Earth, Moscow, 1990.

Greene, J.S. and W.A. Whitaker, Theoretical Calculations of Traveling Ionospheric Disturbances Generated by Low-Altitude Nuclear Explosions, in Acoustic Gravity Waves in the Atmosphere, 1968.

Harvey, D. Seismogram synthesis using normal mode superposition: The locked mode approximation. *Geophy. J.R. Astr. Soc., 66:37-61, 1981.*

Kosloff, D., D. Kessler, A. Filho, E. Tessmer, A. Behle, and R. Strahilevitz. Solution of the equations of dynamic elasticity by a Chebychev spectral method. *Geophysics, 55:734-748, 1990.*

Orrey, J.L. and C.B. Archambeau, Simulating High-Frequency Seismograms in Complicated Media: A Spectral Approach. Proceedings of Conference on Numerical Modeling Methods, DOE, March, 1993.

Orszag, S.A., Numerical simulation of incompressible flows within simple boundaries: I. galerkin (spectral) representation. *Stud. Appl. Math.*, 50:293-327, 1971.

Witte, D.C. and P.G. Richards. The pseudospectral method for simulating wave propagation. *Computational Acoustics,* 3, 1990.

Prof. Thomas Ahrens
Seismological Lab, 252-21
Division of Geological & Planetary Sciences
California Institute of Technology
Pasadena, CA 91125

Prof. Keiiti Aki
Center for Earth Sciences
University of Southern California
University Park
Los Angeles, CA 90089-0741

Prof. Shelton Alexander
Geosciences Department
403 Deike Building
The Pennsylvania State University
University Park, PA 16802

Prof. Charles B. Archambeau
CIRES
University of Colorado
Boulder, CO 80309

Dr. Thomas C. Bache, Jr.
Science Applications Int'l Corp.
10260 Campus Point Drive
San Diego, CA 92121 (2 copies)

Prof. Muawia Barazangi
Institute for the Study of the Continent
Cornell University
Ithaca, NY 14853

Dr. Jeff Barker
Department of Geological Sciences
State University of New York
at Binghamton
Vestal, NY 13901

Dr. Douglas R. Baumgardt
ENSCO, Inc
5400 Port Royal Road
Springfield, VA 22151-2388

Dr. Susan Beck
Department of Geosciences
Building #77
University of Arizona
Tuscon, AZ 85721

Dr. T.J. Bennett
S-CUBED
A Division of Maxwell Laboratories
11800 Sunrise Valley Drive, Suite 1212
Reston, VA 22091

Dr. Robert Blandford
AFTAC/TT, Center for Seismic Studies
1300 North 17th Street
Suite 1450
Arlington, VA 22209-2308

Dr. Stephen Bratt
ARPA/NMRO
3701 North Fairfax Drive
Arlington, VA 22203-1714

Dr. Lawrence Burdick
IGPP, A-025
Scripps Institute of Oceanography
University of California, San Diego
La Jolla, CA 92093

Dr. Robert Burridge
Schlumberger-Doll Research Center
Old Quarry Road
Ridgefield, CT 06877

Dr. Jerry Carter
Center for Seismic Studies
1300 North 17th Street
Suite 1450
Arlington, VA 22209-2308

Dr. Eric Chael
Division [redacted] MS 0655
Sandia Laboratory
Albuquerque, NM 87185-0655

Dr. Martin Chapman
Department of Geological Sciences
Virginia Polytechnical Institute
21044 Derring Hall
Blacksburg, VA 24061

Mr Robert Cockerham
Arms Control & Disarmament Agency
320 21st Street North West
Room 5741
Washington, DC 20451,

Prof. Vernon F. Cormier
Department of Geology & Geophysics
U-45, Room 207
University of Connecticut
Storrs, CT 06268

Prof. Steven Day
Department of Geological Sciences
San Diego State University
San Diego, CA 92182

US Dept of Energy
Recipient, IS-20, GA-033
Office of Rsch & Development
1000 Independence Ave
Washington, DC 20585

Dr. Cliff Frolich
Institute of Geophysics
8701 North Mopac
Austin, TX 78759

Dr. Zoltan Der
ENSCO, Inc.
5400 Port Royal Road
Springfield, VA 22151-2388

Dr. Holly Given
IGPP, A-025
Scripps Institute of Oceanography
University of California, San Diego
La Jolla, CA 92093

Prof. Adam Dziewonski
Hoffman Laboratory, Harvard University
Dept. of Earth Atmos. & Planetary Sciences
20 Oxford Street
Cambridge, MA 02138

Dr. Jeffrey W. Given
SAIC
10260 Campus Point Drive
San Diego, CA 92121

Prof. John Ebel
Department of Geology & Geophysics
Boston College
Chestnut Hill, MA 02167

Dr. Dale Glover
Defense Intelligence Agency
ATTN: ODT-1B
Washington, DC 20301

Eric Fielding
SNEE Hall
INSTOC
Cornell University
Ithaca, NY 14853

Dan N. Hagedon
Pacific Northwest Laboratories
Battelle Boulevard
Richland, WA 99352

Dr. Petr Firbas
Institute of Physics of the Earth
Masaryk University Brno
Jecna 29a
612 46 Brno, Czech Republic

Dr. James Hannon
Lawrence Livermore National Laboratory
P.O. Box 808
L-205
Livermore, CA 94550

Dr. Mark D. Fisk
Mission Research Corporation
735 State Street
P.O. Drawer 719
Santa Barbara, CA 93102

Prof. David G. Harkrider
Seismological Laboratory
Division of Geological & Planetary Sciences
California Institute of Technology
Pasadena, CA 91125

Prof Stanley Flatte
Applied Sciences Building
University of California, Santa Cruz
Santa Cruz, CA 95064

Prof. Danny Harvey
CIRES
University of Colorado
Boulder, CO 80309

Prof. Donald Forsyth
Department of Geological Sciences
Brown University
Providence, RI 02912

Prof. Donald V. Helmberger
Seismological Laboratory
Division of Geological & Planetary Sciences
California Institute of Technology
Pasadena, CA 91125

Dr. Art Frankel
U.S. Geological Survey
922 National Center
Reston, VA 22092

Prof. Eugene Herrin
Institute for the Study of Earth and Man
Geophysical Laboratory
Southern Methodist University
Dallas, TX 75275

Prof. Robert B. Herrmann
Department of Earth & Atmospheric Sciences
St. Louis University
St. Louis, MO 63156

Prof. Lane R. Johnson
Seismographic Station
University of California
Berkeley, CA 94720

Prof. Thomas H. Jordan
Department of Earth, Atmospheric &
Planetary Sciences
Massachusetts Institute of Technology
Cambridge, MA 02139

Prof. Alan Kafka
Department of Geology & Geophysics
Boston College
Chestnut Hill, MA 02167

Robert C. Kemerait
ENSCO, Inc.
445 Pineda Court
Melbourne, FL 32940

Dr. Karl Koch
Institute for the Study of Earth and Man
Geophysical Laboratory
Southern Methodist University
Dallas, Tx 75275

US Dept of Energy
Attn: Max Koontz, NN-20, GA-033
Office of Rsch & Development
1000 Independence Ave, SW
Washington, DC 20585

Dr. Richard LaCoss
MIT Lincoln Laboratory, M-200B
P.O. Box 73
Lexington, MA 02173-0073

Dr. Fred K. Lamb
University of Illinois at Urbana-Champaign
Department of Physics
1110 West Green Street
Urbana, IL 61801

Prof. Charles A. Langston
Geosciences Department
403 Deike Building
The Pennsylvania State University
University Park, PA 16802

Jim Lawson, Chief Geophysicist
Oklahoma Geological Survey
Oklahoma Geophysical Observatory
P.O. Box 8
Leonard, OK 74043-0008

Prof. Thorne Lay
Institute of Tectonics
Earth Science Board
University of California, Santa Cruz
Santa Cruz, CA 95064

Dr. William Leith
U.S. Geological Survey
Mail Stop 928
Reston, VA 22092

Mr. James F. Lewkowicz
Phillips Laboratory/GPEH
29 Randolph Road
Hanscom AFB, MA 01731-3010(2 copies)

Mr. Alfred Lieberman
ACDA/VI-OA State Department Building
Room 5726
320-21st Street, NW
Washington, DC 20451

Prof. L. Timothy Long
School of Geophysical Sciences
Georgia Institute of Technology
Atlanta, GA 30332

Dr. Randolph Martin, III
New England Research, Inc.
76 Olcott Drive
White River Junction, VT 05001

Dr. Robert Masse
Denver Federal Building
Box 25046, Mail Stop 967
Denver, CO 80225

Dr. Gary McCartor
Department of Physics
Southern Methodist University
Dallas, TX 75275

Prof. Thomas V. McEvilly
Seismographic Station
University of California
Berkeley, CA 94720

Dr. Art McGarr
U.S. Geological Survey
Mail Stop 977
U.S. Geological Survey
Menlo Park, CA 94025

Dr. Keith L. McLaughlin
S-CUBED
A Division of Maxwell Laboratory
P.O. Box 1620
La Jolla, CA 92038-1620

Stephen Miller & Dr. Alexander Florence
SRI International
333 Ravenswood Avenue
Box AF 116
Menlo Park, CA 94025-3493

Prof. Bernard Minster
IGPP, A-025
Scripps Institute of Oceanography
University of California, San Diego
La Jolla, CA 92093

Prof. Brian J. Mitchell
Department of Earth & Atmospheric Sciences
St. Louis University
St. Louis, MO 63156

Mr. Jack Murphy
S-CUBED
A Division of Maxwell Laboratory
11800 Sunrise Valley Drive, Suite 1212
Reston, VA 22091 (2 Copies)

Dr. Keith K. Nakanishi
Lawrence Livermore National Laboratory
L-025
P.O. Box 808
Livermore, CA 94550

Prof. John A. Orcutt
IGPP, A-025
Scripps Institute of Oceanography
University of California, San Diego
La Jolla, CA 92093

Prof. Jeffrey Park
Kline Geology Laboratory
P.O. Box 6666
New Haven, CT 06511-8130

Dr. Howard Patton
Lawrence Livermore National Laboratory
L-025
P.O. Box 808
Livermore, CA 94550

Dr. Frank Pilotte
HQ AFTAC/TT
1030 South Highway A1A
Patrick AFB, FL 32925-3002

Dr. Jay J. Pulli
Radix Systems, Inc.
201 Perry Parkway
Gaithersburg, MD 20877

Dr. Robert Reinke
ATTN: FCTVTD
Field Command
Defense Nuclear Agency
Kirtland AFB, NM 87115

Prof. Paul G. Richards
Lamont-Doherty Geological Observatory
of Columbia University
Palisades, NY 10964

Mr. Wilmer Rivers
Teledyne Geotech
314 Montgomery Street
Alexandria, VA 22314

Dr. Alan S. Ryall, Jr.
ARPA/NMRO
3701 North Fairfax Drive
Arlington, VA 22203-1714

Dr. Richard Sailor
TASC, Inc.
55 Walkers Brook Drive
Reading, MA 01867

Prof. Charles G. Sammis
Center for Earth Sciences
University of Southern California
University Park
Los Angeles, CA 90089-0741

Prof. Christopher H. Scholz
Lamont-Doherty Geological Observatory
of Columbia University
Palisades, NY 10964

Dr. Susan Schwartz
Institute of Tectonics
1156 High Street
Santa Cruz, CA 95064

Secretary of the Air Force
(SAFRD)
Washington, DC 20330

Office of the Secretary of Defense
DDR&E
Washington, DC 20330

Thomas J. Sereno, Jr.
Science Application Int'l Corp.
10260 Campus Point Drive
San Diego, CA 92121

Dr. Michael Shore
Defense Nuclear Agency/SPSS
6801 Telegraph Road
Alexandria, VA 22310

Dr. Robert Shumway
University of California Davis
Division of Statistics
Davis, CA 95616

Dr. Matthew Sibol
Virginia Tech
Seismological Observatory
4044 Derring Hall
Blacksburg, VA 24061-04?0

Prof. David G. Simpson
IRIS, Inc.
1616 North Fort Myer Drive
Suite 1050
Arlington, VA 22209

Donald L. Springer
Lawrence Livermore National Laboratory
L-025
P.O. Box 808
Livermore, CA 94550

Dr. Jeffrey Stevens
S-CUBED
A Division of Maxwell Laboratory
P.O. Box 1620
La Jolla, CA 92038-1620

Lt. Col. Jim Stobie
ATTN: AFOSR/NL
110 Duncan Avenue
Bolling AFB
Washington, DC 20332-0001

Brian Stump
Los Alamos National Laboratory
EES-3, Mail Stop C335
Los Alamos, NM 87545

Prof. Jeremiah Sullivan
University of Illinois at Urbana-Champaign
Department of Physics
1110 West Green Street
Urbana, IL 61801

Prof. L. Sykes
Lamont-Doherty Geological Observatory
of Columbia University
Palisades, NY 10964

Dr. David Taylor
ENSCO, Inc.
445 Pineda Court
Melbourne, FL 32940

Dr. Steven R. Taylor
Los Alamos National Laboratory
P.O. Box 1663
Mail Stop C335
Los Alamos, NM 87545

Prof. Clifford Thurber
University of Wisconsin-Madison
Department of Geology & Geophysics
1215 West Dayton Street
Madison, WS 53706

Prof. M. Nafi Toksoz
Earth Resources Lab
Massachusetts Institute of Technology
42 Carleton Street
Cambridge, MA 02142

Dr. Larry Turnbull
CIA-OSWR/NED
Washington, DC 20505

Dr. Gregory van der Vink
IRIS, Inc.
1616 North Fort Myer Drive
Suite 1050
Arlington, VA 22209

Dr. Karl Veith
EG&G
5211 Auth Road
Suite 240
Suitland, MD 20746

Prof. Terry C. Wallace
Department of Geosciences
Building #77
University of Arizona
Tuscon, AZ 85721

Dr. Thomas Weaver
Los Alamos National Laboratory
P.O. Box 1663
Mail Stop C335
Los Alamos, NM 87545

Dr. William Wortman
Mission Research Corporation
8560 Cinderbed Road
Suite 700
Newington, VA 22122

Prof. Francis T. Wu
Department of Geological Sciences
State University of New York
at Binghamton
Vestal, NY 13901

Prof Ru-Shan Wu
University of California, Santa Cruz
Earth Sciences Department
Santa Cruz
, CA 95064

ARPA, OASB/Library
3701 North Fairfax Drive
Arlington, VA 22203-1714

HQ DNA
ATTN: Technical Library
Washington, DC 20305

Defense Intelligence Agency
Directorate for Scientific & Technical Intelligence
ATTN: DTIB
Washington, DC 20340-6158

Defense Technical Information Center
Cameron Station
Alexandria, VA 22314 (2 Copies)

TACTEC
Battelle Memorial Institute
505 King Avenue
Columbus, OH 43201 (Final Report)

Phillips Laboratory
ATTN: XPG
29 Randolph Road
Hanscom AFB, MA 01731-3010

Phillips Laboratory
ATTN: GPE
29 Randolph Road
Hanscom AFB, MA 01731-3010

Phillips Laboratory
ATTN: TSML
5 Wright Street
Hanscom AFB, MA 01731-3004

Phillips Laboratory
ATTN: PL/SUL
3550 Aberdeen Ave SE
Kirtland, NM 87117-5776 (2 copies)

Dr. Michel Bouchon
I.R.I.G.M.-B.P. 68
38402 St. Martin D'Heres
Cedex, FRANCE

Dr. Michel Campillo
Observatoire de Grenoble
I.R.I.G.M.-B.P. 53
38041 Grenoble, FRANCE

Dr. Kin Yip Chun
Geophysics Division
Physics Department
University of Toronto
Ontario, CANADA

Prof. Hans-Peter Harjes
Institute for Geophysic
Ruhr University/Bochum
P.O. Box 102148
4630 Bochum 1, GERMANY

Prof. Eystein Husebye
NTNF/NORSAR
P.O. Box 51
N-2007 Kjeller, NORWAY

David Jepsen
Acting Head, Nuclear Monitoring Section
Bureau of Mineral Resources
Geology and Geophysics
G.P.O. Box 378, Canberra, AUSTRALIA

Ms. Eva Johannisson
Senior Research Officer
FOA
S-172 90 Sundbyberg, SWEDEN

Dr. Peter Marshall
Procurement Executive
Ministry of Defense
Blacknest, Brimpton
Reading FG7-FRS, UNITED KINGDOM

Dr. Bernard Massinon, Dr. Pierre Mechler
Societe Radiomana
27 rue Claude Bernard
75005 Paris, FRANCE (2 Copies)

Dr. Svein Mykkeltveit
NTNT/NORSAR
P.O. Box 51
N-2007 Kjeller, NORWAY (3 Copies)

Prof. Keith Priestley
University of Cambridge
Bullard Labs, Dept. of Earth Sciences
Madingley Rise, Madingley Road
Cambridge CB3 OEZ, ENGLAND

Dr. Jorg Schlittenhardt
Federal Institute for Geosciences & Nat'l Res.
Postfach 510153
D-30631 Hannover , GERMANY

Dr. Johannes Schweitzer
Institute of Geophysics
Ruhr University/Bochum
P.O. Box 1102148
4360 Bochum 1, GERMANY

Trust & Verify
VERTIC
Carrara House
20 Embankment Place
London WC2N 6NN, ENGLAND